Bifold insulating energy scales in the Mott-insulator Ca_2RuO_4

An angle resolve photoemission spectroscopy study

University of Zurich UZH

Denys Sutter

Supervisor: Prof. Dr. Johan Chang

Department of Physics
University of Zurich

This thesis is submitted for the degree of
MSc Physics

August 2016

Acknowledgements

I want to thank Prof. Johan Chang, who gave me this great opportunity to contribute and be part of his research group. Almost on a daily basis, he engaged me in enlightening discussions, challenged and taught me on a high level in all aspects of physical science.

Many thanks to Claudia Fatuzzo for fruitful discussions, helping me out with Matlab and for returning my written drafts in fully red. Also thanks to my office mate Oleh Ivashko for fun intermezzos and his calm attitude and Daniel Destraz, who always was giving honest criticism.

For the realization of this project, I want to especially thank Christian Matt for the small important details of the ARPES technique, Prof. Titus Neupert who contributed tremendously to the theoretical part, Dr. Moritz Hösch who gave extremely valuable feedback in the process of this work and Dr. Simon Moser for deep discussions about matrix element effects.

Many people contributed to the creation of this thesis indirectly, tutors who educated and formed me along my path as a physicist. Especially I would like to thank Prof. Jürg Osterwalder, Dr. Gerson Mette, Dr. Matthias Hengsberger, Prof. Hugo Keller, Prof. René Monnier, Prof. Andreas Schilling and Urs Maier, to whom I am really thankful for their guidance and advice.

I am very happy that I always received full support on all levels from my father Reto, my mother Leah and my sister Lary. Without your support, all this would not have been possible. This year has been very intense, so I am truly grateful for all the shared moments with Catiana. She always was very patient with me and understood it perfectly how to shift my focus when I needed a break. Finally I would like to thank my close friends, *the sharks*, who balance out work on a daily basis. To mention two of them, my room mates Martin and Jascha, I also want to thank them for their support by the collective-mass-studying-effect, which is commonly observed by entering our apartment. For the others, I hope some day I will be able to convince them that research in physics is something exciting and useful ;-).

Summary

A paradigmatic case of multi-band Mott physics including spin-orbit and Hund's coupling is realised in Ca_2RuO_4. Progress to understand the nature of the Mott insulating phase of Ca_2RuO_4 has been impeded by the lack of knowledge about the low-energy electronic structure. In this thesis, it is demonstrated how the band structure of the paramagnetic insulating phase can be measured directly by angle resolved photoemission spectroscopy. The obtained electronic structure features two Mott insulating energy scales. This multi-gap character is analysed through photoemission matrix element effects, band curvature maps and first principle band structure calculations. These results provide detailed insights into the orbital character of the band structure and highlight the multi-band nature of the Mott transition in Ca_2RuO_4.

Zusammenfassung

Ca_2RuO_4 ist ein paradigmatisches Beispiel, in welchem sich Multiband Mott-Physik einschliesslich Spin-Bahn- und Hund'sche-Kopplung manifestiert. Da nur wenig über die niederenergetische, elekronische Struktur von Ca_2RuO_4 bekannt ist, wurde Fortschritt dessen Mott-isolierenden Zustand zu verstehen gebremst. In dieser Abschlussarbeit wird gezeigt, wie die Bandstruktur in der paramagnetischen, isolierenden Phase mittels winkelaufgelöster Photoemissionsspektroskopie gemessen wird. Die elektronische Struktur bringt zwei Mott-isolierende Energieskalen zum Vorschein. Mittels Matrixelementeffekte der Photoemission, Bandkrümmung und *ab initio* Bandstruktur-Rechnungen wird diese Ausprägung analysiert. Die Ergebnisse bieten Einsichten in die orbitalen Charakteren der elektronischen Bänder und verdeutlicht die Multiband-Natur des Mott-Übergangs in Ca_2RuO_4.

Table of contents

Chapter 1

Introduction

Back in *caveman*-times – the Stone Age – human civilization was characterized by the use of tools typically made out of stones. This prehistoric time span ended with the advent of metal working. New materials defined these eras such as in the name giving Bronze Age, the Iron Age and in later periods with the mass production of steel all up to silicon based technology in our current society. Major jumps of technological progress originate ultimately from a better understanding of materials. Nowadays, this field of research is one of the big pillars of modern physics, the *physics of condensed matter*.

Strongly correlated systems

A classic, yet contemporary topic in modern condensed matter physics is the electron correlation problem in transition metal oxides (*TMO*). This class of materials exhibit rich phase diagrams and versatile properties in electronic transport and magnetism. In 1986, the Nobel prize winning discovery of high temperature superconductivity in the cuprates by Georg Bednorz and Karl Alex Müller [1] ignited a new field of research. Further scientific progress has been fueled by the discovery of superconductivity in another layered perovskite, (but copper-free) Sr_2RuO_4 in 1994 by Yoshiteru Maeno [2]. Other breakthroughs in transition metal based materials were achieved by the discovery of colossal magnetoresistance in manganites [3] or the giant thermopower effect in cobaltates [4]. All properties hold great potential for applications.

d electrons in TMO's lead to complicated collective behavior due to the duality of their itinerant and localized nature. Strong correlations are often associated with the proximity to a Mott-insulating state, where electrons are localized due to a strong Coulomb repulsion U. In the past decade it became more and more clear that Hund's coupling J, the intra-atomic exchange interaction, plays a significant role in TMO's displaying strong correlation effects

[5]. A delicate interplay of U and J may lead to complex behavior of orbital and spin degrees of freedom. An example is the compound series $Ca_{2-x}Sr_xRuO_4$. For this family, a rich phase diagram is present [see Fig. 1.1] with unconventional superconductivity[1] in Sr_2RuO_4 on one side ($x = 2$) and the antiferromagnetic Mott-insulator Ca_2RuO_4 on the other ($x = 0$) [6]. It is still an open question what exactly conspires the latter to be Mott insulating, thus the ground state is still controversial. Progress has been held back mainly due to the lack of experimental knowledge of the electronic band structure. This is the main topic of the present thesis.
It is structured by starting with physical concepts, important for Ca_2RuO_4. Then the crystal structure of the compound and possible scenarios for its Mott insulating ground state are discussed. Next, concepts in angle resolved photoemission spectroscopy are introduced, followed by the measurement and discussion of the band structure of Ca_2RuO_4.
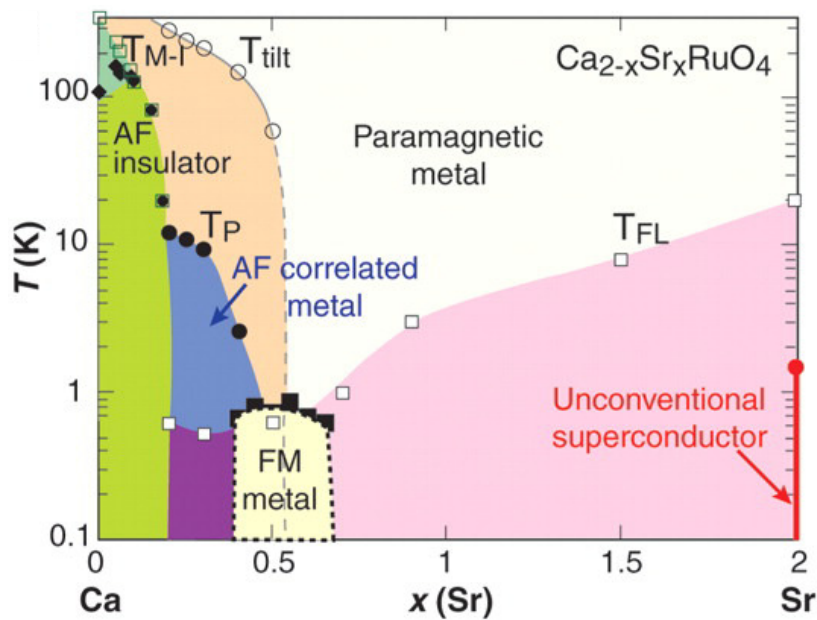
Fig. 1.1 Phase diagram of $Ca_{2-x}Sr_xRuO_4$ [7].

---

[1]triplet pairing of Cooper pairs.

Chapter 2

Physics of the ruthenates

2.1 Mott physics

In band theory, which is based on a one-electron picture in the Hartree-Fock approximation, the distinction between metals and insulators is clear. For insulators the atomic electrons fill up exactly an integer number of bands while all other bands are empty. Occupied and unoccupied bands are seperated by an energy gap except in cases like in the semi-metal Bismuth. Metals exhibit partially filled bands and we can describe low energy excitations as quasiparticles in Landau's Fermi liquid theory [8]. Insulators have an even number, while metals have an odd number of electrons per unit cell. However, some transition metal oxides like NiO with an odd number of electrons per unit cell are insulating [9]. In a half filled valence band, each atomic site is singly occupid. Conducting charge would require at least one electron to hop to a neighboring site, creating an empty orbital and a doubly occupied one. Coulomb repulsion of two electrons occupying the same site might be so strong, that such hopping transitions[1] are too expensive in terms of energy, resulting in localization of the electrons. This was pointed out early on by Nevill Mott and Rudolf Peierls [10]. Such a system becomes a so-called *Mott insulator*. With shrinking lattice constant a[2], orbital overlap increases and a metallic state emerges. This transformation is known as a Mott-Hubbard-transition. The most simple model for d-electrons in transition metals and their compounds is the single-band Hubbard model. The Hamiltonian reads

$$\mathscr{H} = \mathscr{H}_{\text{Band}} + \mathscr{H}_{\text{Coulomb}} = -t \sum_{ij,\sigma} \hat{c}^{+}_{i\sigma} \hat{c}^{-}_{j\sigma} + U \sum_{i} \hat{n}_{i\uparrow} \hat{n}_{i\downarrow} \tag{2.1}$$

---

[1]related to the kinetic energy.

[2]or increasing orbital radial extensions relative to a.

describing nearest neighbor hopping only, via matrix element $-t$, related to the bandwidth $W = 4t$ [Fig. 2.1]. $\hat{c}^{\pm}_{i,\sigma}$ are real-space field operators on the lattice site i with spin σ, $\hat{n}_{i\sigma} = \hat{c}^{+}_{i\sigma}\hat{c}^{-}_{i\sigma}$ is the density operator and U is the matrix element of the Coulomb potential. We focus here on one electron per atomic site (half filling). In the metallic band limit $U = 0$, the band energy is given by a simple Fourier transform:

$$\mathscr{H}_{\text{Band}} = \sum_{\mathbf{k}} \sum_{\sigma} \varepsilon_{\mathbf{k}} \hat{c}^{+}_{\mathbf{k},\sigma} \hat{c}^{-}_{\mathbf{k},\sigma} \tag{2.2}$$

with the dispersion relation:

$$\varepsilon_{\mathbf{k}} = -t \sum_{\mathbf{a}} e^{i\mathbf{k}\cdot\mathbf{a}}, \tag{2.3}$$

where the sum runs over all lattice vectors $\mathbf{a}$ connecting nearest neighbors.
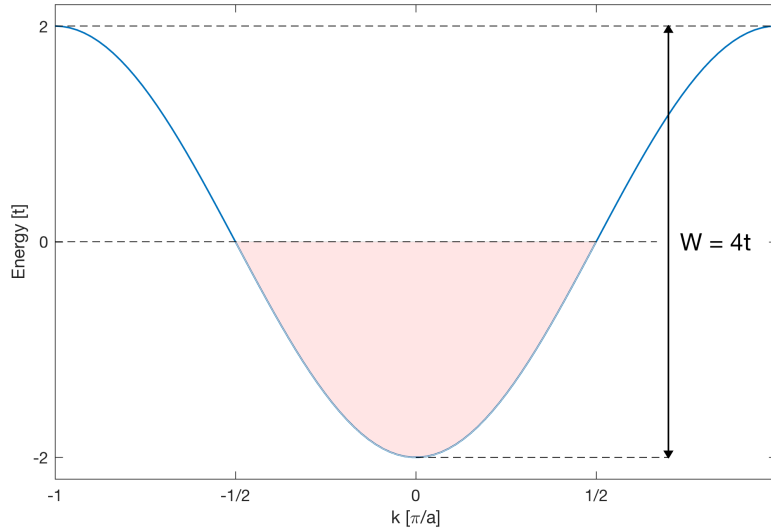
Fig. 2.1 Energy dispersion [eq. (2.3)] of a cubic crystal in one dimension with bandwidth $W = 4t$. Red shaded indicates the band filling.

In the atomic limit $t = 0$ and $U > 0$, the first excitation state has an empty site and one doubly occupied one. This state has energy U, thus the system is an insulator. Suppose we have $N + 1$ electrons where N electrons are localized on their sites. The motion of the extra electron, freely hopping between sites, can be described via an electronic band of width $2t$. By the same token, a hole for $N - 1$ electrons can move freely with bandwidth $2t$. Thus, by starting from the metallic limit and increasing U up to a critical value U_c, we end up with two so-called Hubbard sub-bands of width $W = 2t$, seperated by an energetic Mott-gap Δ. Both extremal cases are summarized in a schematic density of states (Fig. 2.2).
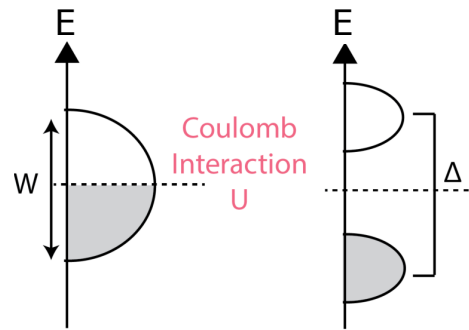
Fig. 2.2 Schematic representation of the density of states of the metal-insulator transition in the Hubbard-model. Starting from metallic half filled band, a strong Coulomb repulsion U splits the band into two Hubbard sub-bands, seperated by a Mott gap.

Despite its simplicity, the single-band Hubbard model is able to describe a variety of phenoma such as itinerant ferromagnetism[3], metal-insulator transition and important aspects of high-T_c superconductivity in layered cuprates.

Starting from a Mott-insulator like La_2CuO_4, superconductivity emerges upon hole or electron doping [11]. This created much attention towards a more elaborate two-dimensional Hubbard model and thus filling-controlled Mott metal-insulator transitions have been studied vividly [12]. An examplified outcome is shown in Fig. 2.3, where the filling is varied by tuning the chemical potential μ:
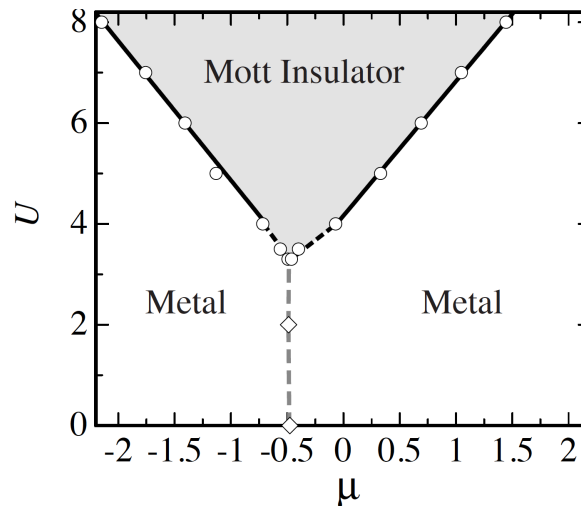

Fig. 2.3 Ground state phase diagram in the plane of U and the chemical potential μ, related to the filling of charge carriers. At $\mu = -0.5$, corresponding to half filling, the Mott insulating phase is most stable. Taken from Watanabe *et al.* [13].

---

[3]the Stoner criterium can be derived.

2.2   Hund's coupling

The Mott phenomenon has been considered as a canonical example of a ground state, driven by strong electron correlations [12]. In general, strongly correlated electron systems such as ruthenates, iron pnictides and chalcogenides are multi-band materials showing strong correlations while not being close to a Mott insulating state. In the past decade, it became more evident that Hund's coupling J may play a significant role and that it introduces an additional channel for electron correlations [5].

Hund's coupling is traditionally associated to intra-atomic exchange coupling: Provided orbitally degenerate states exist, placing electrons in different orbitals reduces the cost in Coulomb energy. Because of the Pauli principle, an antisymmetric orbital wave function requires a symmetric triplet configuration of the electrons. In other words, Hund's coupling aligns the spins of the electronic system. The far reaching consequences of Hund's rule J coupling are very rich and complicated in TMO's, which I would like to illustrate very briefly. A global picture is produced by de' Medici *et al.* [Fig. 2.4] [14]. The basic message is that the strength of J affects the correlated behavior of the electronic system differently, depending on the band filling. For an exact half-filled band, an increase of J decreases the critical U_c for the system to be Mott-insulating dramatically.
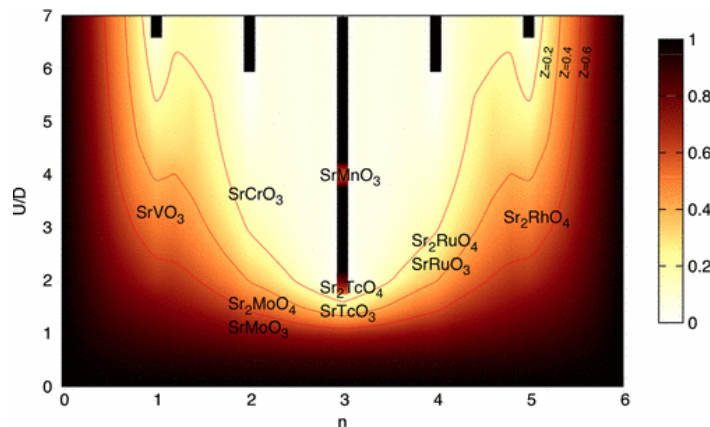
Fig. 2.4 False color plot in the plane of interaction strength U/D and band filling n. D is the bandwidth. The color-code represents the quasiparticle weight Z. J/U is fixed to 0.15. The black bars indicate the Mott-insulating phases. Materials in the plot are placed according to their experimentally determined Z [14].

For one electron (one hole) fillings, J has the opposite effect, driving the system away from the Mott-insulating state. At generic fillings (e.g. $n = 2, 4$), U_c gets enhanced but the quasiparticle weight $Z = m/m^*$ increases with J. The system is further away from a Mott-insulator while being stronger correlated, in the sense of bad-metal behavior. This

includes e.g. a poor ability to screen local moments induced by magnetic impurities[4] or electrical resistivity far above the Mott-Ioffe-limit (mean free path of electrons $\sim$ lattice constant). For a detailed discussion, see a pedagogical review paper by A. Georges *et al.* [5].

2.3 Crystal field

Structural distortions of the lattice crystal structure due to crystal field effects lead to lifted orbital degeneracy and rich physics emerges.

Considering the five d-orbitals in transition-metals with orbital angular momentum quantum numbers $\ell_z = \{-2,...,2\}$ one constructs the wave functions $d_{xy}, d_{xz}, d_{yz}, d_{x^2-y^2}, d_{3z^2-r^2}$ as shown in Fig. 2.5. In perovskite-type TMO's , these transition-metal atoms are surrounded by six O^{-2} ions. The crystal field elevates the energy of the $d_{x^2-y^2}$ and $d_{3z^2-r^2}$ orbitals, extending towards the ligand oxygen ions, with respect to the d_{xy}, d_{xz} and d_{yz} orbitals. The two-fold degenerate subset is called e_g and the three-fold degenerate subset is called t_{2g} with a separation of typical order 1 eV.
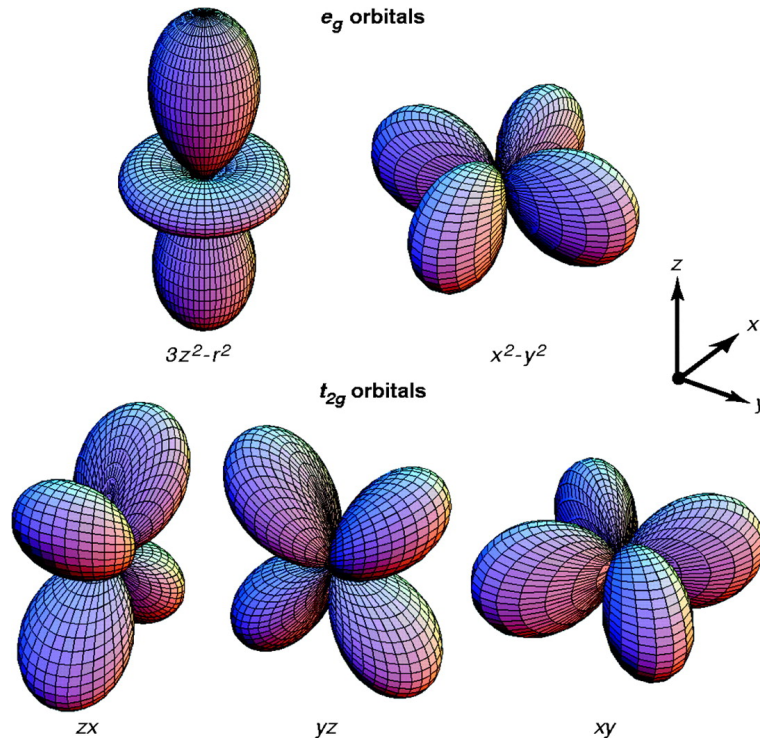

Fig. 2.5 Real space representations of the five d-orbitals as equi-amplitude contour plots [15].

---

[4]This screening effect is attributed to the Kondo problem. A Kondo-temperature scale is associated to it which in turn can be related to a temperature scale for Fermi-liquid behavior.

2.4 Orbital selectivity

Lifting of orbital degeneracy due to the crystal field populates the orbitals differently, leading to orbital polarization. The role of Hund's coupling J is to equalize these orbital populations such that all electrons take advantage of the lowered cost of Coulomb energy. Orbital fluctuations are suppressed so J acts in some aspects as a *band decoupler* [16]. In this sense, J competes with the energy scale of the crystal field. Theoretical studies document that orbital differentiation may lead to exotic orbital-selective Mott phases (*OSMP*), where the orbital manifolds are decoupled and are localized independently. This effects are promoted by Hund's coupling as shown in Fig. 2.6 and discussed in Ref. [17]. It has been suggested that an orbital-selective Mott transition (*OSMT*) is stabilized in systems where the ratio of bandwidths differ strongly from one. The narrow bands get localized before the wide bands. For already small values of J/U, an OSMT can occur for bandwidths of similar magnitude. However, a OSMP is mainly governed by different individual fillings of the bands. Thus, the effect of different band fillings and blockage of orbital fluctuations by Hund's coupling keeps the Hubbard sub-bands and associated Mott-gaps independent [5],[18].
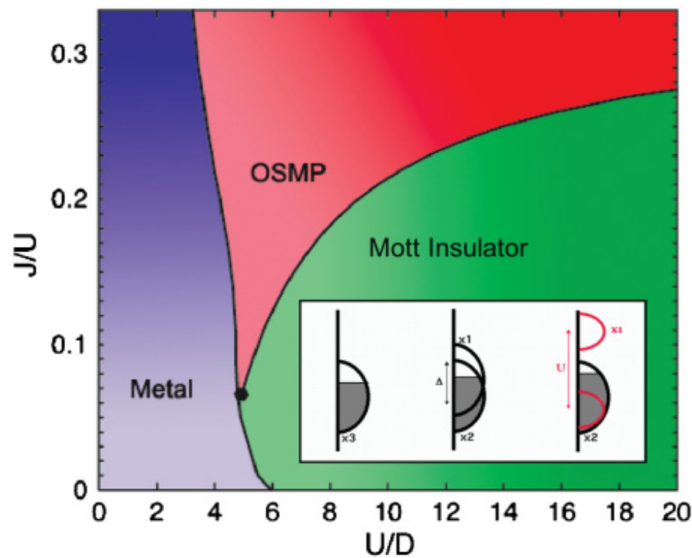
Fig. 2.6 Phase diagram for a three-band Hubbard model populated by four electrons in the J/U-U/D-plane with bandwidth D. The inset shows the DOS of an orbital-selective Mott transition, taken from [18].

The concept of OSMT was initially proposed by V. I. Anisimov *et al.* in order to explain properties of $Ca_{2-x}Sr_xRuO_4$ [6].

2.5 Ca$_{2-x}$Sr$_x$RuO$_4$ series

The discovery of superconductivity in the layered perovskite Sr$_2$RuO$_4$ 1994 by Y. Maeno *et al.*
[2] with $T_c = 0.93\,\text{K}$ [5] has triggered a wide scientific interest in the ruthenates. Fermi-sheets
mapped out by de Haas-van Alphen experiments [20] are in very good agreement with Density
functional theory (*DFT*) calculations in the local density approximation (*LDA*) [21]. Thus,
Sr$_2$RuO$_4$ is a good metal. Isovalent substitution of Sr by Ca-atoms surprisingly suppresses
metallic behavior and turns the compound into an antiferromagnetic Mott-insulator. This
transition is driven by crystallographic distortions such as Jahn-Teller distortions, rotations
and tilt of the RuO$_6$-octahedra [Fig. 2.7], thus narrowing the Ru-4d bands originating from
electrons populating the t_{2g}-manifold [6]. The Ca$_{2-x}$Sr$_x$RuO$_4$ series has been synthesized
and studied in great detail [22]. The phase diagram is showed in Fig. 1.1. In the following,
I will present a few characteristics of the compound family Ca$_{2-x}$Sr$_x$RuO$_4$ for different
degrees of doping x.

Sr$_2$RuO$_4$ ($x = 2$)   Starting with the end member of the series, the superconductor Sr$_2$RuO$_4$[6]
has a tetragonal crystal structure of symmetry group I4/mmm with $a = b = 3.8603\,\text{Å}$ and
$c = 12.729\,\text{Å}$ with RuO$_6$-octahedra slightly elongated along the c-axis.

Paramagnetic metal ($0.5 < x < 2$)   The smaller Ca-ion induces rotations of the octahedra,
starting at $x = 1.5$ which are more pronounced for decreasing x with rotations up to $13°$.

**Antiferromagnetic metal ($0.2 < x < 0.5$)**   At $x = 0.5$ rhombohedral distortions set in
and the octahedra start are slightly tilted. In this region metallic transport coexists with
antiferromagnetic correlations. This inspired V. I. Anisimov *et al.* to propose the orbital-
selective picture of the Mott transition, where the d_{xz} and d_{yz} orbitals are Mott insulating with
antiferromagnetic correlations while the d_{xy} remains metallic [6]. However, this scenario is
still controversial and some experiments are against this picture, e.g. optical conductivity
measurements suggest stronger renormalization effects of d_{xy} quasiparticles leading to
localization [24].

Antiferromagnetic insulator ($0 < x < 0.2$)   Further tilting and compression of the octa-
hedra and thus diminishing bandwidth lead to an insulating ground state. Results from
angle resolved photoemission spectroscopy are controversial. In one study, all Fermi sheets
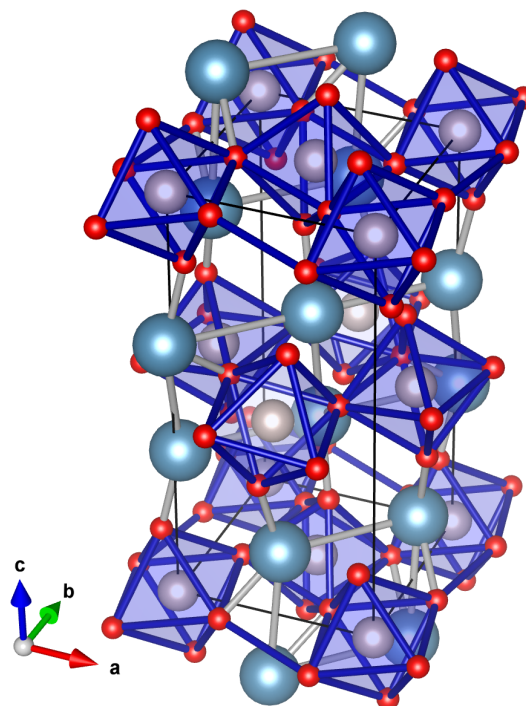are observed [25], while in another study the *xy*-sheet is not seen, as a consequence of the

---

[5]$T_c = 1.5\,\text{K}$ for improved crystal qualities [19] [see Fig. 1.1].
[6]possible p-wave symmetry of the order parameter [23]

orbital-selective nature of $Ca_{1.8}Sr_{0.2}RuO_4$, claimed by the authors [26].
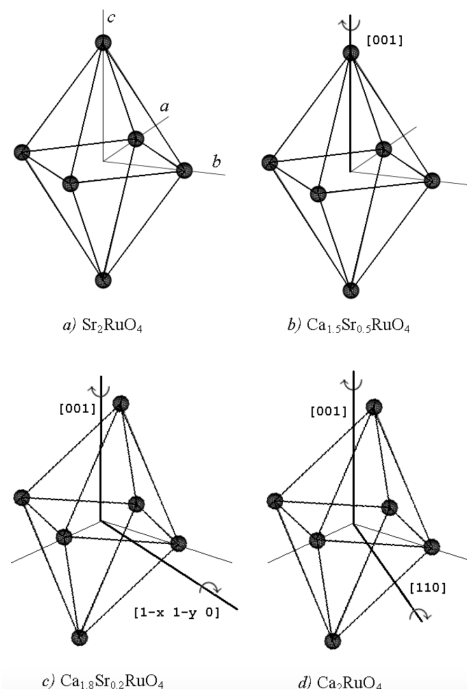
Fig. 2.7 Rotational distortion in $Ca_{2-x}Sr_xRuO_4$ for different x.

Fig. 2.8 Unit cell of Ca_2RuO_4 in the compressed S-Pbca phase. Beige: Ru-atoms, red: O-atoms, blue: Ca-atoms.

Ca_2RuO_4 ($x = 0$)   For the other end member of the series, distortions of the crystal lattice are the strongest in Ca_2RuO_4, with orthorhombic crystal symmetry group Pbca and lattice constants $a = 5.39\,\text{Å}$, $b = 5.59\,\text{Å}$ and $c = 11.77\,\text{Å}$, below $T_s \sim 356\,\text{K}$, where the RuO_6 octahedra are compressed (*S-Pbca*). Above T_s, the octahedra are elongated [27] (*L-Pbca*). Above $T_{AF} \sim 100\,\text{K}$ the compound is a paramagnet, below T_{AF} antiferromagnetism sets in. In the S-Pbca phase (S: short c-axis), the crystal field lowers the energy of the d_{xy}-orbitals. In the limit of extreme compression and $J = 0$, the d_{xy} bands are expected to be filled and band insulating while the d_{xz}- and d_{yz}-orbitals are half-filled. The rotational distortions narrow down the bandwidths such that the latter two bands get Mott localized [6]. This scenario stands in contradiction with X-ray absorption measurements, observing band filling ratios $n_{xy} : (n_{xz} + n_{yz}) = 1 : 3$ at 300 K and $\frac{3}{2} : \frac{5}{2}$ at 90 K and discussed as the result of spin-orbit interaction [28]. Other scenarios have been suggested, see e.g. Ref. [29], [30]. Thus the ground state of Ca_2RuO_4 is still controversial.

Chapter 3

Concepts in photoemission experiments

Even ten years before the electron was discovered by Sir Joseph John Thomson in 1897, Heinrich Hertz observed that an electric spark between two electrodes is more easily created by illuminating them with ultraviolet light [31]. At the beginning of the next century, Philipp Lenard carried out more systematic experiments, investigating the rays produced by irradiating metals. He found that the energy of the rays was independent of the light intensity, but scaled with its frequency [32]. This intriguing result was explained by Albert Einstein in his miraculous year 1905 by introducing the light quantum of energy $h\nu$[33], yielding the equation

$$E_{\mathrm{max}} = h\nu - \Phi \tag{3.1}$$

where E_{max} is the kinetic energy of the fastest emitted electrons and Φ is the *work function* of the metal surface. This relation has been confirmed 1916 by Robert Millikan, thus providing direct measurement of Planck's constant h. With the development of quantum mechanics and theoretical concepts in atomic and solid state physics, the fundamentals for photoelectron spectroscopy has been laid out. In the 1950's Ralph Steinhardt [34] and Kai Siegbahn [35] developed independently *XPS* (x-ray photoelectron spectroscopy) for general chemical analysis. In the following decades powerful probing techniques have been introduced such as *UPS* (ultraviolet photoelectron spectroscopy), *XPD* (x-ray photoelectron diffraction) and *ARPES* (angle resolved photoemission spectroscopy). Recent developments are time resolving pump-probe experiments and spin-resolved ARPES.

3.1 Photoemission process

After Einstein's explanation of the photoelectric effect, sophisticated models contributed to a more profound understanding of the photoemission process. Here I will present the commonly used *three step model*, which has proven to be rather successful, despite its purely phenomenological origin [36] [37] [38].

Step one: Optical excitation of the electron

Time dependent perturbation theory in quantum mechanics predicts electronic transition probabilities for *N*-electron systems upon a perturbation or *interaction* Hamiltonian $\mathscr{H}_{int}(t)$. In the interaction picture[1] of quantum mechanics, it gets clear that transition rates only depend on $\mathscr{H}_{int}(t)$. Considering a finite light wave perturbing a system of *N* charged particles, the Hamiltonian is:

$$\mathscr{H}(t) = \sum_{k=1}^{N} \frac{1}{2m}\left(\mathbf{p}_k - \frac{e}{c}\mathbf{A}(\mathbf{x}_k,t)\right)^2 + V(\mathbf{x}_1,...,\mathbf{x}_N) \equiv \mathscr{H}_0 + \mathscr{H}_{int}(t) \tag{3.2}$$

In the Coulomb gauge $\nabla \cdot \mathbf{A}(\mathbf{x},t) = 0 = -i\hbar\sum_{i=1}^{3}\partial_i A_i = \sum_{i=1}^{3}[p_i, A_i]$:

$$\mathscr{H}_0 = \sum_{k=1}^{N} \frac{1}{2m}\mathbf{p}_k^2 + V(\mathbf{x}_1,...,\mathbf{x}_N) \tag{3.3}$$

$$\mathscr{H}_{int}(t) = -\sum_{k=1}^{N}\frac{e}{mc}\mathbf{A}(\mathbf{x}_k,t)\cdot\mathbf{p}_k + \sum_{k=1}^{N}\frac{e^2}{2mc^2}\mathbf{A}(\mathbf{x}_k,t)^2 \tag{3.4}$$

For wavelengths much larger than the atomic length scale, $\mathbf{A}(\mathbf{x}_k,t)$ is independent of $\mathbf{x}_k$. This is the dipole approximation.

$$\mathbf{A}(\mathbf{x}_k,t)\Psi_0^N(\mathbf{x}_1,...,\mathbf{x}_N) \approx \mathbf{A}(0,t)\Psi_0^N(\mathbf{x}_1,...,\mathbf{x}_N) \tag{3.5}$$

In this fashion, the last part in $\mathscr{H}_{int}(t)$ is a constant and is not relevant. This leads to:

$$\mathscr{H}_{int}(t) = -\frac{e}{mc}\mathbf{A}(0,t)\cdot\sum_k\mathbf{p}_k = -\frac{1}{c}\mathbf{A}(0,t)\cdot\frac{i}{\hbar}[\mathscr{H}_0,\mathbf{P}], \qquad \mathbf{P} = e\sum_{k=1}^{N}\mathbf{x}_k \tag{3.6}$$

with electric dipole operator $\mathbf{P}$, commutation relation $\frac{i}{\hbar}[\mathscr{H}_0,\mathbf{x}_k] = \frac{\mathbf{p}_k}{m}$ and the matrix element $\langle\Psi_f^N|[\mathscr{H}_0,\mathbf{P}]|\Psi_i^N\rangle = \hbar(\omega_i - \omega_f)\langle\Psi_f^N|\mathbf{P}|\Psi_i^N\rangle$.

---

[1]also known as the Dirac picture.

The absorption of a photon of energy $h\nu$ excites an initial state $|\Psi_i^N\rangle$ of energy E_i^N to a final state $\langle\Psi_f^N|$ of energy E_f^N. Assuming a harmonic perturbation the transition rate is derived, known as *Fermi's golden rule*:

$$\Gamma_{i\to f} = \frac{2\pi}{\hbar}|\langle\Psi_f^N|\mathscr{H}_{\text{int}}|\Psi_i^N\rangle|^2\delta(E_f^N - E_i^N - h\nu) \qquad (3.7)$$

It is convenient to factorize the N-particle state into a single photoelectron state $|\phi^k\rangle$ and a $N-1$ particle state $|\Psi^{N-1}\rangle$. Since the system will relax after the excitation process and will screen the photohole, introducing complex behaviour, we make use of the *sudden approximation*. As the name suggests, we assume the photoemission process to be sudden (instantaneous electron removal), with no further interactions between the free photoelectron and the $N-1$ electron system accompanied by a discontinuous change of its effective potential. To account for proper Fermion-spin-statistics we use the orthogonal projector A to antisymmetrize the product states:

$$|\Psi_\alpha^N\rangle = A(|\phi_\alpha^k\rangle\otimes|\Psi_\alpha^{N-1}\rangle), \qquad \alpha = \{i,f\} \qquad (3.8)$$

This approximation is valid for high kinetic energies of the photoelectrons but has proven its validity even to some degree for kinetic energies down to 20 eV in cuprate high-temperature superconductors (HTSC) [39]. For the initial state we use this factorized form by means of a Slater determinant in the Hartree-Fock formalism. We define the photoelectron dipole matrix element $\mathscr{M}_{i,f} \equiv \langle\phi_k|\mathscr{H}_{\text{int}}|\phi_k\rangle$ and decompose the $N-1$ final state into its eigenstate components $\Psi_f^{N-1} = \sum_m \Psi_{f,m}^{N-1}$ with the overlap integrals $c_{m,i} = \langle\Psi_m^{N-1}|\Psi_i^{N-1}\rangle$. The total photoemission intensity $I(\mathbf{k},E_{\text{kin}}) \propto \sum_{i,f}\Gamma_{i\to f}$ is proportional to:

$$I(\mathbf{k},E_{\text{kin}}) \propto \sum_{i,f}|\mathscr{M}_{i,f}|^2\sum_m|c_{m,i}|^2\delta(E_{\text{kin}} + E_m^{N-1} - E_i^N - h\nu) \qquad (3.9)$$

In solids with strong electronic correlations the removal of the photoelectron results in a strong change of the effective potential such that Ψ_i^{N-1} overlaps with many eigenstates Ψ_m^{N-1}. A rigorous determination of the $c_{m,i}$'s would be complicated and inefficient. In the framework of *many-body perturbation theory* a slightly different expression has been developed to describe quasiparticle excitations near the Fermi level:

$$I(\mathbf{k},E_{\text{kin}}) \propto \sum_{i,f}|\mathscr{M}_{i,f}^{\mathbf{k}}|^2 \times \mathscr{A}(\mathbf{k},E) \times f(T,E) \qquad (3.10)$$

where $\mathscr{A}(\mathbf{k_f}, E)$ is the so-called one particle spectral function which will be discussed in the following chapter and $f(T,E) = \frac{1}{e^{(E-E_F)/k_B T}+1}$ is the Fermi-Dirac-function describing fermionic statistics for state occupation below the Fermi energy E_F.

Step two: Propagation of the photoelectrons to the surface

When the optically excited photoelectron travels to the surface, it can suffer various inelastic scattering events. In general the mechanisms at play during transport is highly complicated and is object of present research, e.g. here at the University of Zurich in the group of Prof. Jürg Osterwalder, ultrafast electron dynamics is studied by pump-probe spectroscopy, resolving processes in the attosecond time scale. Here we shall describe inelastic scattering interactions in a simplified fashion by the so-called *universal curve* for the inelastic mean free path λ_{IMFP}, which turns out to be nearly material independent. In the present ARPES study we use photon energies in the range of $h\nu = 30 - 120$ eV corresponding to an escape depth of order $\lambda_{\mathrm{IMFP}} \sim 5$ Å, thus dealing with extreme surface sensitivity.

.
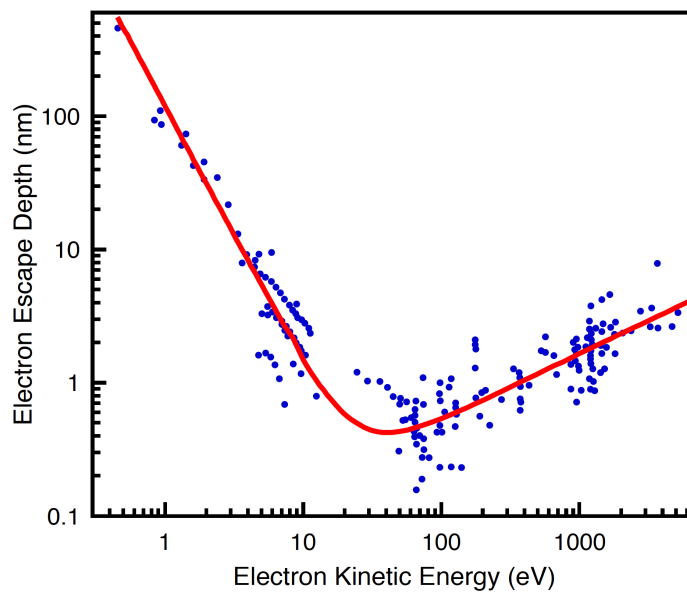
Fig. 3.1 Plot of the universal curve of the inelastic mean free path as a function of kinetic energy. Figure taken from [40]

The short probe depth is comparable to the layer spacing in TMO's, solidifying the validity of the sudden approximation.

## Step three: Transmission of the photoelectrons into vacuum

A fundamental difficulty in ARPES is how the wave vector $\mathbf{k}$ at the detector relates to $\mathbf{k}_{int}$ of the photoelectron inside the crystal. This problem arises from the fact that only the kinetic energy of the electron is measured and not its momentum [41].

The transmission process must obey energy and momentum conservation, dictating for the kinetic energy of the photoelectrons with binding energy E_B:

$$E_{kin} = h\nu - E_B - \Phi \tag{3.11}$$

Together with detector angles θ, φ [Fig. 3.2] the wave vector of a free electron in vacuum can be defined:

$$\mathbf{k} = \frac{1}{\hbar}\sqrt{2mE_{kin}} \times (\sin\theta\cos\varphi, \sin\theta\sin\varphi, \cos\theta) \tag{3.12}$$
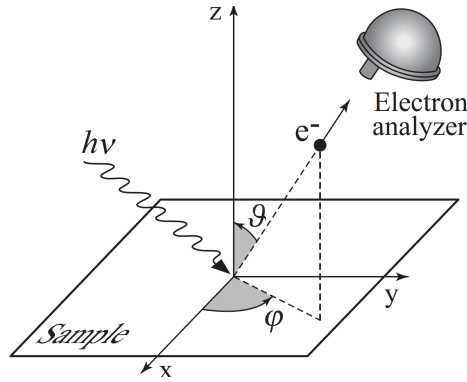
Fig. 3.2 Illustration of the setup geometry with the angles as indicted [42]

As the dispersion $\varepsilon_{\mathbf{k}_{int}}$ of the photoelectron inside the solid is in general unknown, derivation of $\mathbf{k}_{int}$ is not possible. In addition, the photoelectron has to overcome the surface barrier resulting in refraction. In this process, the periodic crystal potential ensures conservation of the parallel components $\mathbf{k}_{\parallel} = \mathbf{k}_{int,\parallel}$. Perpendicular to the surface, translation symmetry of the crystal potential is broken by a potential step $-V_0$ in the solid to 0 in vacuum. V_0 arises as a mean potential, that the photoelectron has to overcome. The complexity of this problem is reduced in the so-called *free electron final state approximation*, where the photoelectron is treated as a single plane wave such that:

$$\mathbf{k}_{int} = \frac{1}{\hbar}\sqrt{2m(E_{kin} + V_0)} \times (\sin\theta_{int}\cos\varphi, \sin\theta_{int}\sin\varphi, \cos\theta_{int}) \tag{3.13}$$

where θ_{int} is the internal polar angle in the crystal. These relations imply immediately that for photons with higher energies, we are able to probe higher Brillouin zones (*BZ*), thus increasing $k_{int,z}$ when $\mathbf{k}_{int,||}$ is fixed. Furthermore, the conservation of $\mathbf{k}_{||}$ leads to exact mapping of the energy dispersion of two-dimensional systems like for the Shockley surface state on a clean Cu(111) surface [43].

3.2 Many-body physics

In order to describe elementary excitations in real solids, many body perturbation theory has been proven as a useful tool in solid state physics [44]. The main idea is to consider the response of an electronic system as a whole, upon removal/addition of an electron from/to a single particle state. The response is given in terms of the complex and energy dependent *self energy* $\Sigma(\mathbf{k}, E)$, which describes screening effects and finite lifetime of quasiparticle excitations $\tau \sim \frac{\hbar}{2\Im m \Sigma(\mathbf{k},E)}$. Instead of solving the Kohn-Sham equations in density functional theory, a more general set of equations have to be solved:

$$\left(-\frac{\hbar^2}{2m}\nabla^2 + V(\mathbf{x}) \right) f_s(\mathbf{x}) + \int \Sigma(\mathbf{x}, \mathbf{x}', E_s) f_s(\mathbf{x}') \, \mathrm{d}\mathbf{x}' = E_s f_s(\mathbf{x}) \tag{3.14}$$

The exited state with quantum number *s*, is described by the so-called *quasiparticle* amplitude $f_s(\mathbf{x})$. A natural way to find practical approximations to the self energy are one-electron addition (+) and removal (-) Green's functions for interacting electrons $G^{\pm}(\mathbf{k}, E)$. They describe the time evolution of an extra added electron / hole due to ionization of the system.

To briefly introduce the concept of the Green's function, we start with the time-dependent Schrödinger equation for a single electron in an external potential $V(\mathbf{x}, t)$ and free particle Hamiltonian $\mathscr{H}_0 = -\frac{\hbar^2}{2m}\nabla^2$:

$$\left(\frac{\hbar}{i} \frac{\partial}{\partial t} + \mathscr{H}_0(\mathbf{x}) \right) \psi(\mathbf{x}, t) = -V(\mathbf{x}, t) \psi(\mathbf{x}, t) \tag{3.15}$$

The Green's function $G_0(\mathbf{x}, \mathbf{x}', t)$ satisfies the equation

$$\left(\frac{\hbar}{i} \frac{\partial}{\partial t} + \mathscr{H}_0(\mathbf{x}) \right) G_0(\mathbf{x}, \mathbf{x}', t) = -\delta(\mathbf{x} - \mathbf{x}') \delta(t) \tag{3.16}$$

$G_0(\mathbf{x}, \mathbf{x}', t)$ is the Fourier transform of $G_0(\mathbf{x}, \mathbf{x}', E)$:

$$G_0(\mathbf{x}, \mathbf{x}', t) = \frac{1}{2\pi\hbar} \int_{-\infty}^{+\infty} G_0(\mathbf{x}, \mathbf{x}', E) e^{-iEt/\hbar} \, \mathrm{d}E \tag{3.17}$$

It can be shown that $G_0(\mathbf{x}, \mathbf{x}', E)$ is the real space representation of the projection operator with eigenfunctions $\{\phi_i(\mathbf{x})\}$ of $\mathcal{H}_0(\mathbf{x})$ and associated eigenvalues $\{\varepsilon_i^0\}$:

$$G_0^+(\mathbf{x}, \mathbf{x}', E) = \sum_i \frac{\langle \mathbf{x} | \phi_i \rangle \langle \phi_i | \mathbf{x}' \rangle}{E - \varepsilon_i^0 + i\eta}, \qquad \eta > 0 \tag{3.18}$$

where a positive infinitesimal η is introduced to handle the poles on the real axis. From eq. (3.18) it is clear that eigenstates of the system corresponds to the poles of the Green's function. The Fourier transform [eq. (3.17)] can now be computed as a contour integral in the lower half complex plane[2]. Eq. (3.15) can now formally be solved:

$$\psi(\mathbf{x}, t) = \phi(\mathbf{x}, \mathbf{t}) + \int G_0^+(\mathbf{x}, \mathbf{x}', t - t') V(\mathbf{x}', t') \psi(\mathbf{x}', t') \, d\mathbf{x}' \, dt' \tag{3.19}$$

The concept of Green's functions can be expanded to systems of interacting electrons. Similar to eq. (3.18), one finds:

$$G^{\pm}(\mathbf{k}, E) = \sum_m \frac{|\langle \Psi_m^{N\pm1} | \hat{c}_\mathbf{k}^{\pm} | \Psi_i^N \rangle|^2}{E \mp (E_m^{N\pm1} - E_i^N) \pm i\eta} \tag{3.20}$$

But now, the amplitudes are matrix elements of electron creation $\hat{c}_\mathbf{k}^+$ and annihilation $\hat{c}_\mathbf{k}^-$ between many-body states. The one-electron addition and removal spectra $\mathscr{A}^{\pm}(\mathbf{k}, E)$ describe the single particle excitation spectrum:

$$\mathscr{A}^{\pm}(\mathbf{k}, E) = \sum_m |\langle \Psi_m^{N\pm1} | \hat{c}_\mathbf{k}^{\pm} | \Psi_i^N \rangle|^2 \delta(E - E_m^{N\pm1} + E_i^N) \tag{3.21}$$

Using the representation of the delta distribution

$$\delta(x - x_0) = \lim_{\eta \to 0^+} \frac{\mp 1}{\pi} \Im \frac{1}{x - x_0 \pm i\eta}, \tag{3.22}$$

the one-electron spectral function $\mathscr{A}(\mathbf{k}, E) = \mathscr{A}(\mathbf{k}, E)^+ + \mathscr{A}(\mathbf{k}, E)^-$ reads:

$$\mathscr{A}(\mathbf{k}, E) = -\frac{1}{\pi} \Im G(\mathbf{k}, E) \tag{3.23}$$

with $G(\mathbf{k}, E) = G^+(\mathbf{k}, E) + [G^-(\mathbf{k}, E)]^*$. By virtue of eq. (3.14), the Green's function satisfies:

$$\left(-\frac{\hbar^2}{2m} \nabla^2 + V(\mathbf{x}) - E \right) G(\mathbf{x}, \mathbf{x}', E) + \int \Sigma(\mathbf{x}, \mathbf{x}'', E) G(\mathbf{x}'', \mathbf{x}', E) \, d\mathbf{x}'' = -\delta(\mathbf{x} - \mathbf{x}') \tag{3.24}$$

---

[2]For negative times, the contour has to be closed in the upper half plane to converge. Since it contains no poles, the result is $G_0(\mathbf{x}, \mathbf{x}', t) = 0$.

In operator form:

$$(\mathscr{H}_0 + V - E)G(E) + \Sigma(E)G(E) = -\mathbf{1} \tag{3.25}$$

Taking diagonal matrix elements in the basis of Bloch functions with band index n, wave vector $\mathbf{k}$ and using eq. (3.23) we obtain:

$$G(\mathbf{k}, E) = \frac{1}{E - \varepsilon_{n\mathbf{k}} - \Sigma(\mathbf{k}, E)}, \tag{3.26}$$

$$\mathscr{A}(\mathbf{k}, E) = -\frac{1}{\pi} \frac{\mathfrak{Im}\Sigma(\mathbf{k}, E)}{[E - \varepsilon_{n\mathbf{k}} - \mathfrak{Re}\Sigma(\mathbf{k}, E)]^2 + [\mathfrak{Im}\Sigma(\mathbf{k}, E)]^2} \tag{3.27}$$

where $\varepsilon_{n\mathbf{k}}$ is the bare band dispersion, $\mathfrak{Re}\Sigma(\mathbf{k}, E)$ contains energy renormalization effects while $\mathfrak{Im}\Sigma(\mathbf{k}, E)$ accounts for the inverse lifetime of the photohole. When interactions are absent like in a free electron gas, the spectral function is simply a delta distribution. In real solids however, the spectral function is broadened and consists of a coherent and an incoherent part [Fig. 3.3].
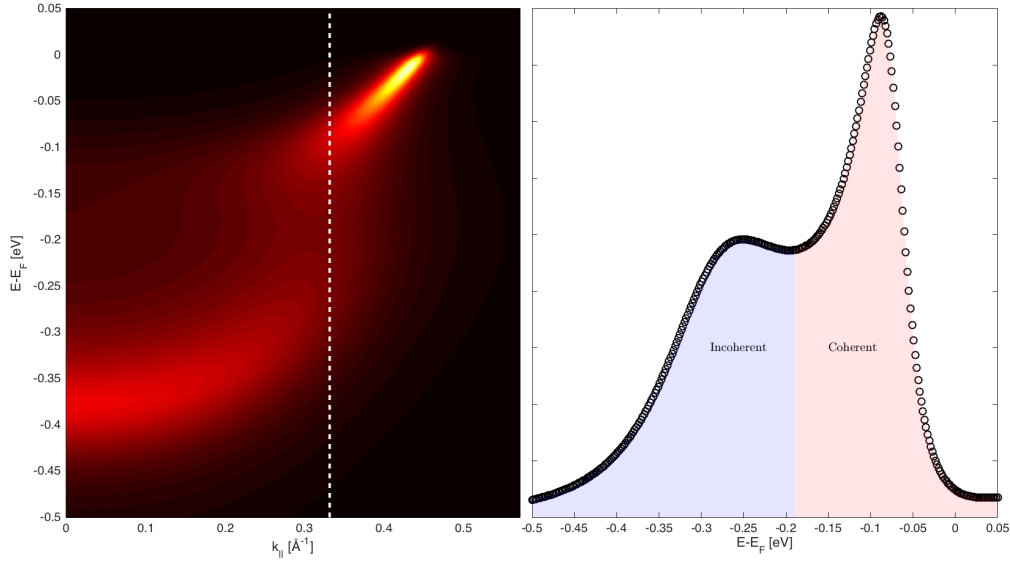
Fig. 3.3 Left: False color plot of the spectral function in a toy model with strong correlations. Right: Energy distribution curve (spectral cut as indicated by the white dashed line) displaying a coherent quasiparticle peak near the Fermi level E_F and an incoherent part towards higher excitation energies.

Recalling eq. (3.28):

$$I(\mathbf{k}, E_{\text{kin}}) \propto \sum_{i,f} |\mathscr{M}_{i,f}^{\mathbf{k}}|^2 \times \mathscr{A}(\mathbf{k}, E) \times f(T, E), \tag{3.28}$$

the spectral function is the meeting point of many-body physics and the ARPES experiment.

3.3 Matrix element effects

Depending on the experimental geometry, light polarization and photon energy, spectra can reveal asymmetric spectral weight distributions which from experimentalists are often referred as *matrix element effects*. I would like to present two approaches to extract information out of matrix element effects.

A · p – approach

Fermis Golden rule eq. 3.7 and the representation of the interaction Hamiltonian eq. 3.6 lead to a transition rate with matrix element:

$$\mathscr{M}_{if} \sim \langle \phi_f | \mathbf{A} \cdot \mathbf{p} | \phi_i \rangle = -i\hbar \langle \phi_f | \mathbf{A} \cdot \nabla | \phi_i \rangle \sim \langle \phi_f | \mathbf{D} \cdot \nabla | \phi_i \rangle \tag{3.29}$$

where the vector potential $\mathbf{A}$ is related to the polarization vector $\mathbf{D}$. For a general experimental configuration, $\mathbf{D}$ can be written in Jones notation

$$\mathbf{D} = D e^{i\lambda} \begin{pmatrix} \cos \varepsilon \\ e^{i\delta} \cos \theta_\ell \sin \varepsilon \\ e^{i\delta} \sin \theta_\ell \sin \varepsilon \end{pmatrix} \tag{3.30}$$

where ε is the ratio of the components of $\mathbf{D}$. $\varepsilon = 0$ defines σ- and $\varepsilon = \pi/2$ defines π-polarization. δ is a relative phase. $\delta = \pm\pi/2$ and $\varepsilon = \pi/4$ are set for right-handed circular (+) and left handed (-) circular light polarization. θ is the angle between beam and surface normal. λ is an overall phase, which is canceled in the modulus squared of the matrix element.

In the following, I outline the main ideas of S. Mosers derivations [45]. Initial states are approximated as atomic orbitals $|\phi_i\rangle \sim |nlm\rangle$ and the final state as a plane wave $\langle \mathbf{x}|\phi_f\rangle \sim \langle \mathbf{x}|\mathbf{k}_f\rangle = e^{i\mathbf{k}_f \cdot \mathbf{x}}$. The first step is to integrate by parts [3]:

---

[3] vanishing boundary terms due to localized nature of initial states.

$$\langle \mathbf{k}_f | \mathbf{D} \cdot \nabla | \phi_i \rangle = \int d\mathbf{x}\, e^{-i\mathbf{k}_f \cdot \mathbf{x}} \mathbf{D} \cdot \nabla \phi_{nlm}(\mathbf{x}) = +i\mathbf{D} \cdot \mathbf{k}_f \int d\mathbf{x}\, e^{-i\mathbf{k}_f \cdot \mathbf{x}} \phi_{nlm}(\mathbf{x}) \qquad (3.31)$$

In this fashion, the matrix element is essentially proportional to the Fourier transform of the orbitals.

$$\mathscr{M}_{if} \propto \mathbf{D} \cdot \mathbf{k}_f \langle \mathbf{k}_f | nlm \rangle \qquad (3.32)$$

The next level of complexity is a tight binding approach, where the initial state wave function is a linear combination of atomic orbitals $\sim \sum_{\mathbf{R}_j} \sum_{nml} c_{j,nml}(\mathbf{k}) | \mathbf{R}_j, nlm \rangle$ located at each site $\mathbf{R}$. $c_{j,nlm}$ are tight binding coefficients and $| \mathbf{R}_j, nlm \rangle$ are atomic wave functions at coordinates $\mathbf{R}_j$ within one unit cell. Summing up over all lattice sites, the matrix element is now proportional to:

$$
\begin{aligned}
\mathscr{M}_{if} &\propto \sum_{\mathbf{R}} e^{i\mathbf{k} \cdot \mathbf{R}} \sum_{\mathbf{R}_j} \sum_{nml} c_{j,nlm}(\mathbf{k}) \langle \mathbf{k}_f | \mathbf{R} + \mathbf{R}_j, nlm \rangle \\
&= \sum_{\mathbf{R}} e^{i(\mathbf{k} - \mathbf{k}_f) \cdot \mathbf{R}} \sum_{\mathbf{R}_j} \sum_{nml} c_{j,nlm}(\mathbf{k}) \langle \mathbf{k}_f | \mathbf{0} + \mathbf{R}_j, nlm \rangle \\
&= \frac{N}{V} \underbrace{\int d\mathbf{R}\, e^{i(\mathbf{k} - \mathbf{k}_f) \cdot \mathbf{R}}}_{\propto \delta(\mathbf{k} - \mathbf{k}_f)} \sum_{\mathbf{R}_j} \sum_{nlm} c_{j,nlm}(\mathbf{k}) e^{-i\mathbf{k} \cdot \mathbf{R}_j} \langle \mathbf{k}_f | \mathbf{0}, nml \rangle
\end{aligned}
$$

Leading to an expression including a term with the shape of a form factor $\sum_{\mathbf{R}_j} e^{i\mathbf{k}_f \cdot \mathbf{R}_j}$. The matrix element is:

$$\mathscr{M}_{if} \propto \sum_{\mathbf{R}_j} \sum_{nlm} c_{j,nlm}(\mathbf{k}_f) e^{-i\mathbf{k}_f \cdot \mathbf{R}_j} M_{nlm}(\mathbf{k}_f) \qquad (3.33)$$

$\mathbf{A} \cdot \mathbf{x}$ – approach

This model has been used to compare the results qualitatively with ARPES spectra of $3d$-orbitals in iron pnictide superconductors [46]. According to eq. 3.6, the matrix element $\mathscr{M}_{if} \equiv \mathscr{M}$ may also be written as:

$$\mathscr{M} \propto \langle \phi_f | \mathscr{H}_{\text{int}} | \phi_i \rangle \sim \langle \phi_f | \mathbf{A} \cdot \mathbf{x} | \phi_i \rangle \sim \langle \phi_f | \mathbf{D} \cdot \mathbf{x} | \phi_i \rangle \qquad (3.34)$$

Initial states $| \phi_i \rangle$ are atomic orbitals and final states $\langle \phi_f |$ are plane waves. In real space representation, an expansion in partial waves is useful:

$$\langle \mathbf{x} | \phi_i \rangle = \psi_{n\ell m}(r, \theta, \varphi) = R_{n\ell}(r) Y_\ell^m(\theta, \varphi) \tag{3.35}$$

$$\langle \mathbf{x} | \phi_f \rangle = \langle \mathbf{x} | \mathbf{k}_f \rangle = e^{i\mathbf{k}_f \cdot \mathbf{x}} = 4\pi \sum_{\ell=0}^{\infty} \sum_{m=-\ell}^{\ell} i^\ell j_\ell(k_f r) Y_\ell^{m*}(\theta_k, \varphi_k) Y_\ell^m(\theta, \varphi) \tag{3.36}$$

where $R_{n\ell}(r)$ is the radial part of the wavefunction, $Y_\ell^m(\theta, \varphi)$ are spherical harmonics and $j_\ell(kr)$ are spherical Besselfunctions. For a fixed magnetic quantum number $m = \lambda$, the associated matrix element $\mathcal{M}^\lambda$ is:

$$\mathcal{M}^\lambda(\theta_k, \varphi_k) \propto \langle \mathbf{k}_f | \mathbf{D} \cdot \mathbf{x} | \phi_i \rangle = \int_{\mathbb{R}^3} d\mathbf{x} \, \langle \mathbf{k}_f | \mathbf{D} \cdot \mathbf{x} | \mathbf{x} \rangle \langle \mathbf{x} | \phi_i \rangle = \int_{\mathbb{R}^3} d\mathbf{x} \, \langle \mathbf{k}_f | \mathbf{x} \rangle \mathbf{D} \cdot \mathbf{x} \langle \mathbf{x} | \phi_i \rangle =$$

$$= \sum_{\ell=0}^{\infty} (-i)^\ell 4\pi \int_0^\infty dr \, r^2 R_{n'\ell'}(r) j_\ell(k_f r)(D_x x + D_y y + D_z z) \times$$

$$\times \sum_{m=-\ell}^{\ell} Y_\ell^m(\theta_k, \varphi_k) \oint_{S^2} d\Omega Y_\ell^{m*}(\theta, \varphi) Y_{\ell'}^\lambda(\theta, \varphi) \equiv$$

$$\equiv D_x \Upsilon_x^\lambda(\theta_k, \varphi_k) + D_y \Upsilon_y^\lambda(\theta_k, \varphi_k) + D_z \Upsilon_z^\lambda(\theta_k, \varphi_k)$$

where $\Upsilon_{\alpha=\{x,y,z\}}^\lambda(\theta_k, \varphi_k)$ denote the matrix element components associated with the spherical harmonic $Y_{\ell'}^\lambda$ which is weighted with the polarization of the light D_α at given emission angles θ_k, φ_k [Fig. 3.4]. By defining $p_\alpha = \alpha/r$ with $\alpha = \{x, y, z\}$ as spherical harmonics

$$p_x = x/r = \sqrt{\frac{1}{2}}\left(Y_1^{-1} - Y_1^1\right), \quad p_y = y/r = i\sqrt{\frac{1}{2}}\left(Y_1^{-1} + Y_1^1\right), \quad p_z = z/r = Y_1^0, \tag{3.37}$$

$\Upsilon_\alpha^\lambda(\theta_k, \varphi_k)$ can be expressed as:

$$\Upsilon_\alpha^\lambda(\theta_k, \varphi_k) = \sum_{\ell=0}^{\infty} (-i)^\ell 4\pi \overbrace{\int_0^\infty dr \, r^3 R_{n'\ell'}(r) j_\ell(k_f r)}^{\rho_\ell(k_f r)} \times \tag{3.38}$$

$$\times \sum_{m=-\ell}^{\ell} Y_\ell^m(\theta_k, \varphi_k) \overbrace{\oint_{S^2} d\Omega Y_\ell^{m*}(\theta, \varphi) p_\alpha Y_{\ell'}^\lambda(\theta, \varphi)}^{f_\alpha^\lambda(\ell, m)} \tag{3.39}$$

where $f_\alpha^\lambda(\ell,m)$ are standard Gaunt coefficients which have only non-vanishing components for $\ell = 1,3$. Summarizing:

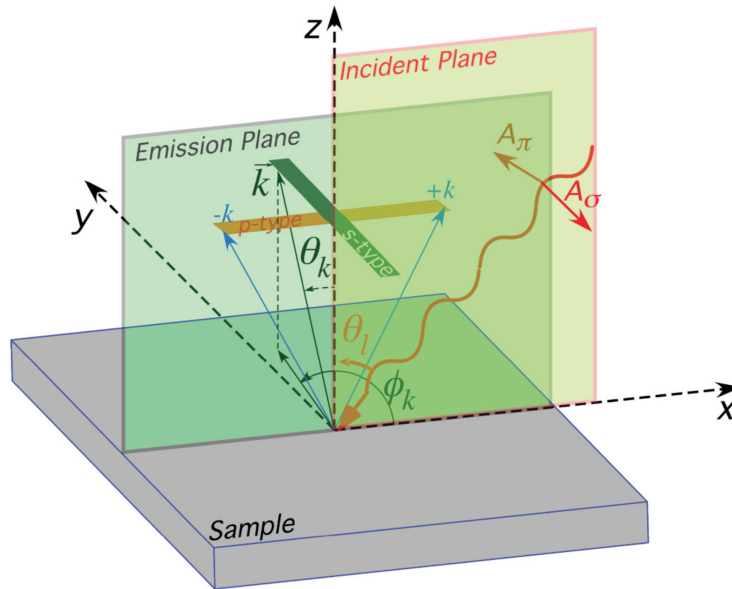$$\mathscr{M}^\lambda(\theta_k,\varphi_k) = \sum_{\alpha=x,y,z} \mathscr{M}_\alpha^\lambda(\theta_k,\varphi_k) = \sum_{\alpha=x,y,z} D_\alpha \Upsilon_\alpha^\lambda(\theta_k,\varphi_k) \tag{3.40}$$

To obtain real space orbital related matrix elements (for d_{yz}, d_{xz}, d_{xy}) we use the relations:

$$\mathscr{M}_{d_{yz}} = i\sqrt{\frac{1}{2}}\left(\mathscr{M}^{-1} + \mathscr{M}^1\right)$$

$$\mathscr{M}_{d_{xz}} = \sqrt{\frac{1}{2}}\left(\mathscr{M}^{-1} - \mathscr{M}^1\right) \tag{3.41}$$

$$\mathscr{M}_{d_{xy}} = i\sqrt{\frac{1}{2}}\left(\mathscr{M}^{-2} - \mathscr{M}^2\right)$$

A phenomenological phase $e^{i\gamma}$ is added to the z-component, which is further discussed in the appendix. For the orbital δ, we conclude with:

$$\mathscr{M}_\delta = \mathscr{M}_{\delta,x} + \mathscr{M}_{\delta,y} + \mathscr{M}_{\delta,z} \cdot e^{i\gamma} \tag{3.42}$$


Fig. 3.4 Sketch of the experimental setup. The light polarization vector is expressed by the incident angles ϕ_ℓ and θ_ℓ. The angles ϕ_k and θ_k are given by the detector slit geometry. Figure taken from [46].

3.4   Sample preparation

For the rest of the thesis, I solely focus on the compound Ca_2RuO_4 (*Ca214*). High quality single crystals were grown by R. Fittipaldi and A. Vecchione at Univesità di Salerno in Italy. The flux-feeding floating-zone technique was used. In this process, polycrystals are melted locally and subsequently solidified in a single crystalline form. At the same time, impurities are carried away as the molten zone is moved along the crystal. Synthesis of Ca214 followed a recipe outlined by S. Nakatsuji and Y. Maeno [47]. Quality in terms of crystallinity at room temperature was checked by Laue X-ray diffraction.

Prior to our ARPES experiments, the crystals were glued on a phosphor-bronze sample holder using electrically conducting, two component silver epoxy paste (EPO-TEK E4110). The silver epoxy cured over night using a heating plate which stabilized a curing temperature of $\sim 75°C$, just below the phase transition temperature T_s. Usage of conducting glue is crucial to electrically ground the sample. Since in the photoemission process electrons are removed from the material, an insulating sample is prone to charge up electrostatically. In an ARPES spectra this induces unwanted shifts of the Fermi level which is typically sensitive to the incident photon flux. The silver epoxy provides an electronic and mechanical connection of the sample to an electron reservoir, sample holder. All samples were then aligned by using a Laue X-ray diffractometer in order to identify crystallographic axes. This process also allowed a quality check of the sample batch by comparing how clear the diffraction patterns are. A typical Laue-pattern with the X-ray beam along the crystal *c*-axis is shown in Fig. 3.5.
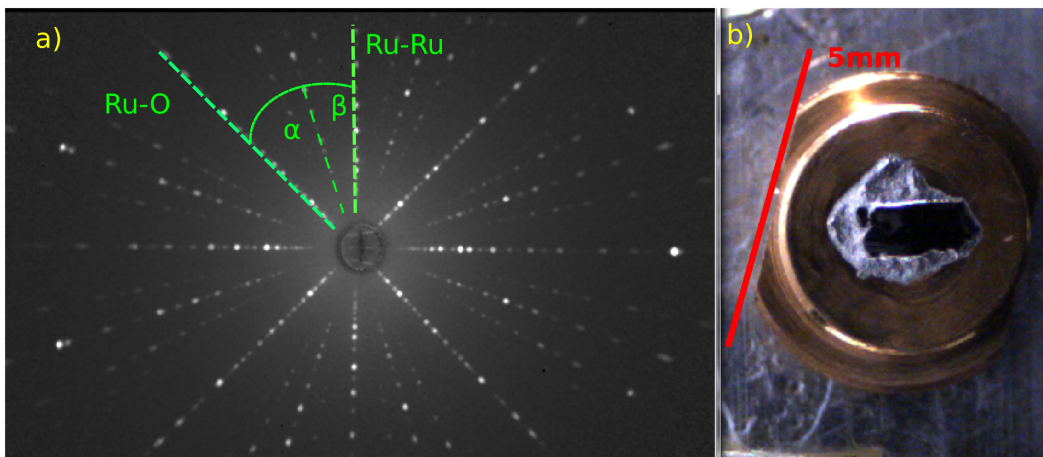
Fig. 3.5 a) Laue diffraction pattern of Ca_2RuO_4 in the $a - b$-plane with angles $\alpha > \beta$ as indicated. b) Typical sample (black) positioned corresponding to the diffraction pattern. Courtesy: Bachelor-thesis, F. Cossalter.

By identifying the indicated angles, a distinction of the Ru-O or Ru-Ru bonds is possible. Hence, the Laue diffractometer allows orientation of the crystals. After orienting the samples, a cylindrical post ($d = 1$mm, $\ell = 6$mm) is glued on top of each crystal surface. During the experiment, the sample are in an ultra high vacuum environment with a base pressure of order $5 \times 10^{-9} - 1 \times 10^{-10}$ mbar and cooled down to $T = 150$ K[4]. Hitting away the top-post may cleave the sample. This cleaving process is often used for layered crystal structures, since it removes the topmost layers and a clean surface is left behind. Typically in one out of three cleave attempts, the quality of the sample surface is good enough to measure the band structure with ARPES as presented later on.

3.5 Experimental setup

All ARPES experiments were carried out at external synchrotron facilities. In the following they are introduced and I show how the detector channels of the energy analyzer are calibrated.

Synchrotron facilities

The most obvious advantage of synchrotron light compared to conventional gas-discharge lamps like He-lamps or laser sources is the possibility to tune the photon energy over a wide range at a high intensity and to change polarization of the incident light: parallel to the plane spanned by the light and surface normal (π), perpendicular to it (σ) or circular. Generic synchrotron facilities consist of a large electron storage ring. Radiation is produced by accelerating electrons in so-called insertion devices or undulators. The desired photon energy is selected by a grating monochromator. The beam is then focused on the sample.
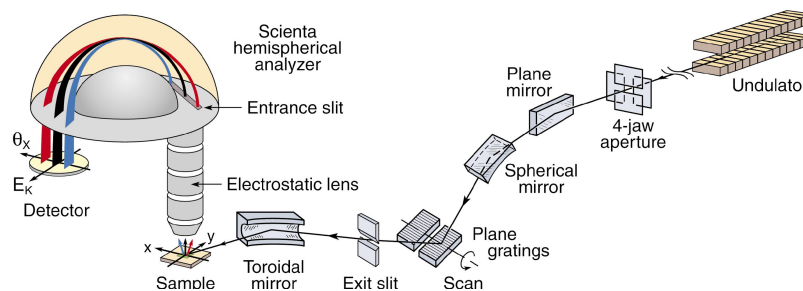
Fig. 3.6 Typical ARPES beamline at a synchrotron light source [42]. Electrons traversing the undulator, a periodic magnet structure, undergo oscillations and radiate. The beam gets optimized by optics and is brought onto the sample. Emitted photoelectrons are then detected by the analyzer.

[4]paramagnetic insluting S-Pbca phase of Ca_2RuO_4.

Experiments were carried out at the Surface and Interface Spectroscopy (SIS) beamline at the Swiss Light Source (SLS) at the Paul Scherrer Institute (PSI), at the I05 beamline at Diamond Light Source Ltd. (DLS) near Oxford, UK and at the MAESTRO beamline at the Advanced Light Source (ALS) in the Berkeley labs, US [Table 3.1].

	I05 (DLS)	SIS (SLS)	MAESTRO (ALS)
Photon spot size	$< 50 \times 50 \, \mu\mathrm{m}^2$	$< 50 \times 100 \, \mu\mathrm{m}^2$	$< 10 \times 10 \, \mu\mathrm{m}^2$
Energy resolution (in energy range used)	$5 - 10 \, \mathrm{meV}$	$\sim 10 \, \mathrm{meV}$	$\sim 10 \, \mathrm{meV}$
Angular resolution	$\sim 0.1°$	$\sim 0.15°$	$\sim 0.1°$
Photon energies	$18 - 240 \, \mathrm{eV}$	$10 - 800 \, \mathrm{eV}$	$20 - 1000 \, \mathrm{eV}$
Temperatures	$10 - 300 \, \mathrm{K}$	$10 - 300 \, \mathrm{K}$	$< 12 - 400 \, \mathrm{K}$

Table 3.1 Table summarizing endstation properties of the beam lines used.

Detector calibration

State-of-the-art, commercially available hemispherical energy analyzers (Scienta R4000) were used in all our experiments. They consist of two metallic hemispheres with a voltage applied between them. An incoming electron beam is focused by electrostatic lenses and follows a trajectory according to their kinetic energy. High energetic electrons hit the upper hemisphere, while the low energetic electrons are captured by the lower one. Tuning the applied voltage selects the desired kinetic energy with a chosen pass energy. At the other end of the analyzer, the electrons are typically detected by a CCD chip with several hundred channels resolving an angular range of $\sim -15°$ to $15°$.
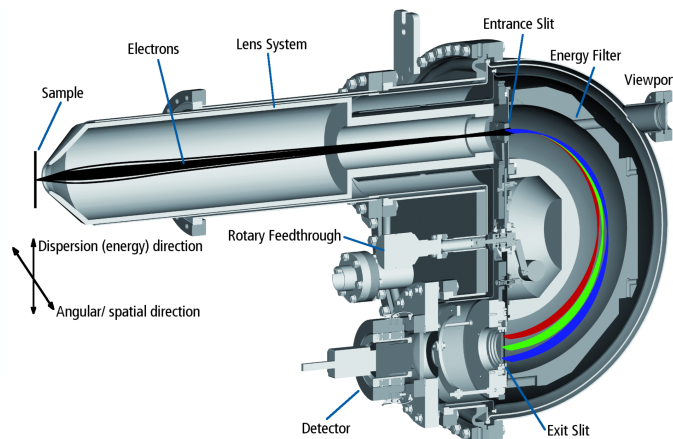

Fig. 3.7 Cross-section of a typical hemispherical energy analyzer, taken from [48].

Before the data analysis can start, one has to take care of a proper normalization of the measured signal. We performed this reference measurements on polycrystaline copper or on a gold coated surface. First of all, the efficiency of the detector channels vary strongly and can depend also on the photon energy. The integrated intensities are a good measure for the relative detector efficiencies, thus providing the possibility to normalize each channel n:

$$I_{norm.}(n, E_B) = \frac{I_{meas.}(n, E_B)}{\sum_{E_B} I_{Au}(n, E_B)} \tag{3.43}$$
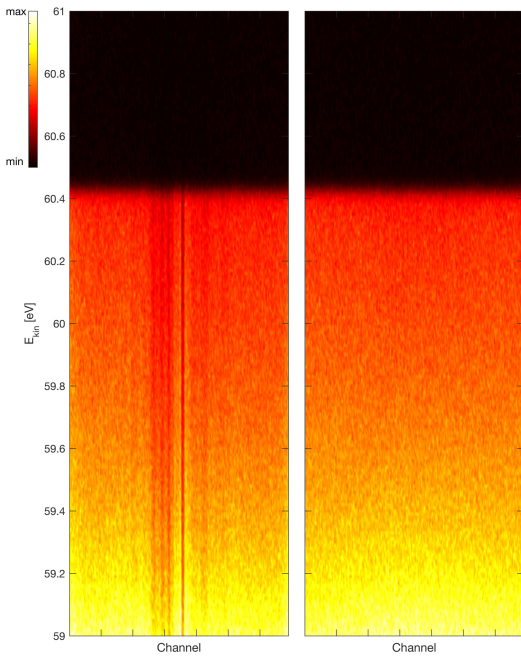
Fig. 3.8 ARPES measurements taken on polycrystalline gold. The axes are the kinetic energy vs. detector channels. Intensities are indicated by the colorcode. Left: Raw detector intensities, Right: Normalized detector intensities.
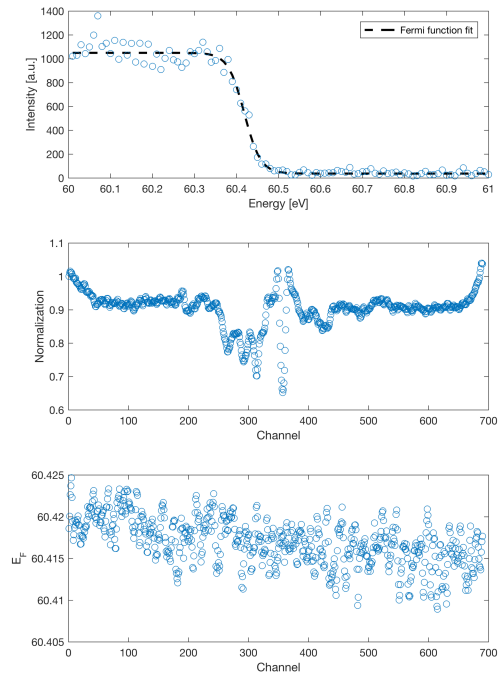
Fig. 3.9 Top: Fermi tail and fit for a selected channel. Middle: Total efficiency per channel, normalized representation with respect to channel 1. Bottom: Fermi energy for all channels.

To display spectra on a binding energy scale we can fit the end of the spectrum by a Fermi-Dirac (FD) distribution in the reference measurement and determine the Fermi energy in each channel. We then define the energy scale:

$$-E_B = E_{kin} - E_F \tag{3.44}$$

Note that with this procedure, this scale only holds for the sample when it is in thermodynamical and electrical equilibrium with the reference material. In an ARPES ex-

periment, the electrons leave the sample with a kinetic energy $h\nu - E_B - \Phi_{\text{sample}}$. When they penetrate the detector material with workfunction Φ_{det}, they gain the energy difference (assuming $\Phi_{\text{det}} < \Phi_{\text{sample}}$). Thus, yielding a sample independent energy scale with $E_{kin} = h\nu - E_B - \Phi_{\text{sample}} + (\Phi_{\text{sample}} - \Phi_{\text{det}}) = h\nu - E_B - \Phi_{\text{det}}$. The calibration procedure is summarized in Fig. 3.9.

Due to the high collimation of the synchrotron light, the momentum resolution is not the limitation. With a photon energy of $h\nu = 50\,\text{eV}$ and an angular resolution of $1.5°$ we resolve $\sim 1/50$ of a BZ. The energy resolution of standard hemispherical analyzers improved over time down to $5 - 10\,\text{meV}$. The total experimental energy resolution ΔE_{exp} can be estimated fitting the Fermi-Dirac distribution and use $T_{FD} = \sqrt{T_{\text{sample}}^2 + (\Delta E_{\text{exp}}/4k_B)^2}$. This yields a total energy resolution of $\sim 40\,\text{meV}$ in our experiments. In Ca214, the insulating energy scales are larger than the energy resolution. Energy resolution is also not a limiting factor.

3.6 Data analysis

Modern energy analyzers in ARPES experiments collect data simultaneously resolving energy and momentum. It is convenient however, to analyze the energy distribution maps (*EDM*) with cuts through the intensity map.
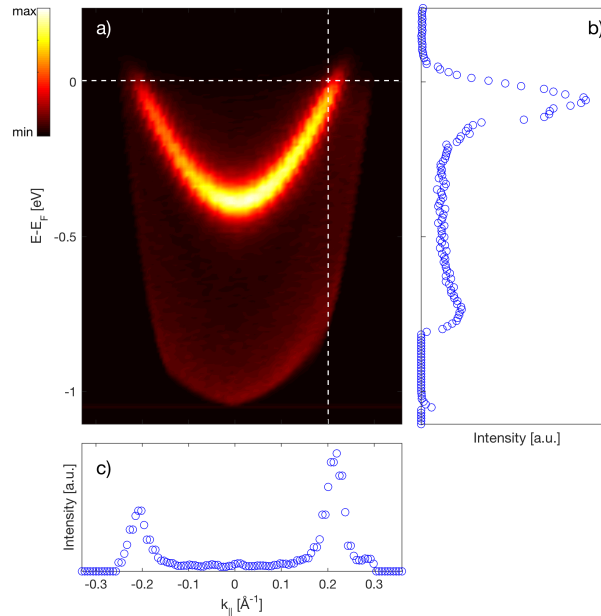
Fig. 3.10 a) ARPES energy distribution map of the Shockley surface state on a Cu(111) surface. b) and c) corresponding energy distribution curve and momentum distribution curve along horizontal and vertical whited dashed lines. Data taken from [43].

Intensity as a function of momentum at fixed binding energy are called momentum distribution curves (*MDC*). Intensity as a function of binding energy at fixed momentum are called energy distribution curves (*EDC*) [Fig. 3.10].

MDC

Symmetric lineshapes and the simple background makes an MDC easier to analyze than an EDC. In the limit of momentum independent self energy, the spectral function takes the simple form of a Lorentzian [49],

$$\mathscr{A}(\omega) = -\frac{1}{\pi} \frac{\mathfrak{Im}\Sigma(\omega)}{[\hbar\omega - \varepsilon_{\mathbf{k}} - \mathfrak{Re}\Sigma(\omega)]^2 + [\mathfrak{Im}\Sigma(\omega)]^2}, \tag{3.45}$$

centered around $\varepsilon_{\mathbf{k}} = \hbar\omega - \mathfrak{Re}\Sigma(\omega)$ and full width at half maximum $\Gamma = 2\mathfrak{Im}\Sigma(\omega) \propto \tau^{-1}(\omega)$, proportional to the inverse lifetime of the photohole. A relation for the mean free path λ is obtained with

$$\lambda = \Delta k^{-1} = \frac{\hbar v_{\mathbf{k}}}{2\mathfrak{Im}\Sigma(\omega)} \tag{3.46}$$

where $v_{\mathbf{k}}$ it the bare band velocity. For a fixed energy $\hbar\omega$, the intensity in a MDC reads:

$$I^{\mathrm{MDC}}(k) \propto \frac{\Delta k}{[\hbar\omega - \varepsilon_{\mathbf{k}} - \mathfrak{Re}\Sigma(\omega)]^2 + \Delta k^2}, \tag{3.47}$$

As a general note, for anisotropic systems with commonly rather complex Fermi surfaces, $\Sigma(\omega)$ is not momentum independent. However, the energy dependence should still dominate over the momentum dependence of e.g. electron-phonon coupling contributions as demonstrated in the charge density wave system 2H-TaSe$_2$ [50].

EDC

As mentioned, the self energy $\Sigma(\omega)$ typically stronger dependent on energy rather than momentum. This is reflected in the energy dependent inverse lifetime $\tau^{-1}(\omega)$, leading to asymmetric lineshapes. The intensity in an EDC reads:

$$I^{\mathrm{EDC}}(\omega) = \frac{\mathfrak{Im}\Sigma(\omega)}{[\hbar\omega - \varepsilon_{\mathbf{k}} - \mathfrak{Re}\Sigma(\omega)]^2 + [\mathfrak{Im}\Sigma(\omega)]^2} \times f(T, \omega) \tag{3.48}$$

Quasiparticle excitations spectra near the Fermi level are influenced by the Fermi-Dirac distribution $f(T, \omega)$.

Conversion of detector angles into k-space

One has to be clear, that in an ARPES experiment, the data provided by the energy analyzer is a 3-tensor in case of a constant energy map[5] or a matrix in case of 2D-spectra[6]. In order to display the intensity maps properly in k-space, the angles have to be transformed in the spirit of equation (3.12). Besides translation, the used manipulators have three rotational degrees of freedom. This is illustrated in Fig. 3.11 and demonstrated as follows.
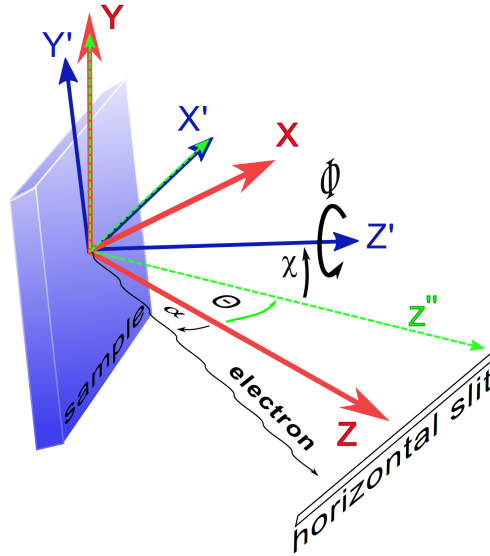
Fig. 3.11 Sketch of the rotational degrees of freedom of a typical ARPES manipulator. Figure taken from [51].

Let us start with the intrinsic (blue) coordinate system x', y', z' of the manipulator aligned with the laboratory coordinate system (red) x, y, z. For now, it is assumed that the crystallographic axes a, b, c are congruent with the manipulator axes as well. The analyzer slit lies in the xz plane with α denoting the detector angle (rotation around y). In this initial configuration the momentum of the photoelectron is:

$$\mathbf{k} = \frac{1}{\hbar} \sqrt{2mE_{kin}} \begin{pmatrix} -\sin\alpha \\ 0 \\ \cos\alpha \end{pmatrix} \tag{3.49}$$

For an arbitrary angular setting of the manipulator, the rotations are described by Θ (around y), χ (around x') and Φ (around z').

---

[5]kinetic energy, detector channel angle, tilt angle and intensity
[6]kinetic energy, detector channel angle and intensity

$$R_\Theta = \begin{pmatrix} \cos\Theta & 0 & -\sin\Theta \\ 0 & 1 & 0 \\ \sin\Theta & 0 & \cos\Theta \end{pmatrix}, R_\chi = \begin{pmatrix} 1 & 0 & 0 \\ 0 & \cos\chi & \sin\chi \\ 0 & -\sin\chi & \cos\chi \end{pmatrix}, R_\Phi = \begin{pmatrix} \cos\Phi & -\sin\Phi & 0 \\ \sin\Phi & \cos\Phi & 0 \\ 0 & 0 & 1 \end{pmatrix}$$

To account for the common case, that the crystal c-axis is misaligned with respect to the manipulator z'-axis, the final adjustment is done with rotations γ (mismatch c-axis and z'-axis) and β (angle between a-axis and x'-axis).

$$R_\gamma = \begin{pmatrix} \cos\gamma & 0 & -\sin\gamma \\ 0 & 1 & 0 \\ \sin\gamma & 0 & \cos\gamma \end{pmatrix}, R_\beta = \begin{pmatrix} \cos\beta & -\sin\beta & 0 \\ \sin\beta & \cos\beta & 0 \\ 0 & 0 & 1 \end{pmatrix}$$

The transformed momentum $\mathbf{k}'$ of the photoelectron is

$$\mathbf{k}' = R_\beta R_\gamma R_{-\beta} R_\Phi R_\chi R_\Theta \mathbf{k} \tag{3.50}$$

In this fashion manipulator angles are translated into momentum space.

Curvature method

In order to enhance dispersive features in 2D intensity maps, usually second derivatives are applied. However, a big drawback is a resulting shift of the intensity maxima. Zhang *et al.* demonstrated a significant improvement of this method in both accuracy and visualization [52]. Instead of the Laplacian $\nabla^2 f(x,y) = \frac{\partial^2 f}{\partial x^2} + \frac{\partial^2 f}{\partial y^2}$ of a two dimensional function $f(x,y)$, the curvature $C(x,y)$ is a measure how strong a function curves:

$$C(x,y) \sim \frac{[1 + C_x(\frac{\partial f}{\partial x})^2]C_y\frac{\partial^2 f}{\partial y^2} - 2C_x C_y \frac{\partial f}{\partial x}\frac{\partial f}{\partial y}\frac{\partial^2 f}{\partial x \partial y} + [1 + C_y(\frac{\partial f}{\partial y})^2]C_x\frac{\partial^2 f}{\partial x^2}}{[1 + C_x(\frac{\partial f}{\partial x})^2 + C_y(\frac{\partial f}{\partial y})^2]^{\frac{3}{2}}} \tag{3.51}$$

where C_x and C_y are arbitrary constants, which tune the contrast in x or y direction. In Fig. 3.12 the curvature function projects out the maximum very sharp and accurately. Only distortions can be observed near intersections or near the beginning and the end of spectral lines like near the Fermi cutoff. Very recent, the curvature method found its application in several other ARPES studies [53] [54] and will be also used in the presented work. Preliminary processing starts with noise filtering of the data, because equation (3.51) peaks at the smallest plateaus of $f(x,y)$. Noise filtering can be done with a Gaussian filter. A

more sophisticated method is transforming the data into the wavelet domain, then cutting
out high frequency contributions and transforming back the data. Compared to Fourier-
transformations, where the basis are sines and cosines, wavelets have the advantage of being
local. In this fashion, filtering an area of a 2D map does not affect and filter another area.
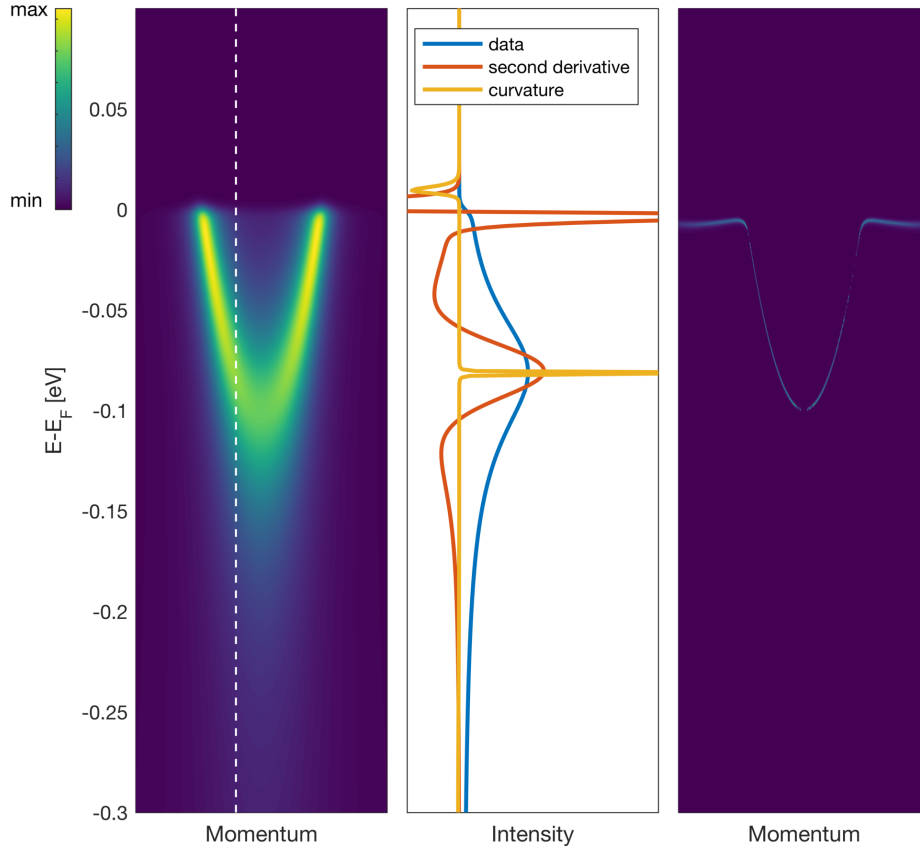
Fig. 3.12 Left: Toy model of a spectral function times the Fermi-Dirac function. The blue dashed line
marks the true maximum for the EDC, indicated by the white dashed line. Middle: EDC with second
derivative and curvature. Right: 2D curvature map of a).

In an ARPES study by Campuzano *et al.* [55], Debauchies wavelets have been used for
this purpose. Here I used throughout the Coiflet wavelets, providing a better mean square
error and signal to noise ratio [56]. It is to emphasize that curvature maps cannot replace
ordinary MDC and EDC analysis of ARPES spectra because the rich information stored in the
shape of the data related to intrinsic scattering processes and other fundamental interactions
is completely lost. Hence, this method is meant as a complimentary visualization tool.

Chapter 4

Band structure of Ca$_2$RuO$_4$

Very little is known about the bandstructure of Ca$_2$RuO$_4$ (Ca214). Angle integrated photoemission spectroscopy has revealed the existence of Ru-states with binding energy 1.6 eV [28]. In a recent resonant inelastic x-ray scattering study of Ca214 in the antiferromagnetic ground state suggest that spin-orbit interaction plays a significant role in shaping the magnetic moments [57]. In the following, I present an ARPES study of the band structure of Ca214 in the paramagnetic insulating state ($T = 150$ K). In general, rotational distortions of TMO-octahedra [see Fig. 4.1] induce Umklapp-potentials which are typically weak. From this follows that in reciprocal space, signatures of band folding are weak as well. In the experimental ARPES community, one traditionally discusses high symmetry points of the Brillouin zone (BZ) in tetragonal notation [26]. Here we actually observe band folding very clearly and thus introduce orthorhombic notation of the BZ in our results.
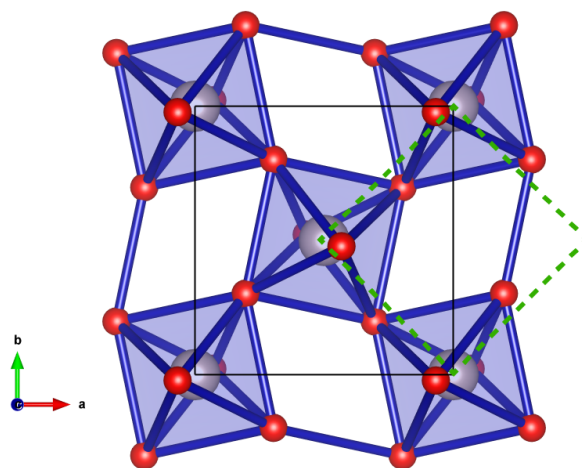

Fig. 4.1 Top view of the unit cell of Ca$_2$RuO$_4$. Orthorhombic distortions doubles the unit cell from tetragonal structure (dashed, green boundary) to the orthorhombic structure (straight, black boundary).

Experimental data are compared to first-principle DFT+LDA calculations including spin-orbit interaction and a tunable self-energy $\Sigma(\omega)$ in the Mott insulating regime.

4.1   Oxygen bands

In Fig. 4.2 a typical ARPES spectra along the $S-X$ high symmetry direction is shown. Two set of bands are observed. Closer to the Fermi-level, the electronic band structure is dominated by the Ruthenium bands. Below $\varepsilon \lesssim -2.8\,\text{eV}$ with $\varepsilon \equiv E - E_F$ oxygen bands take over and are observed down to higher energies $\varepsilon = -7\,\text{eV}$. Along the zone boundary, band features of high degeneracy are found at the S-points for $\varepsilon \sim -5.2\,\text{eV}$.
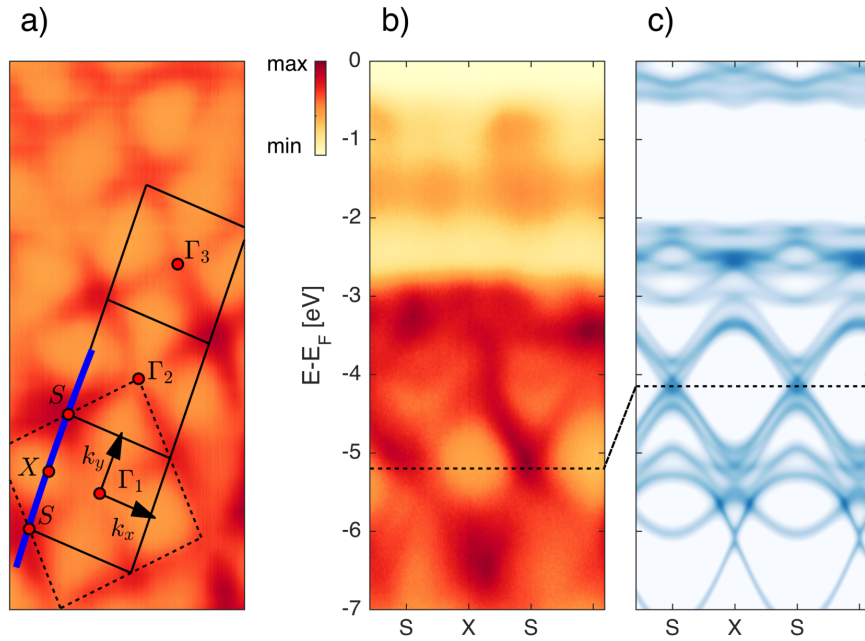

Fig. 4.2 ARPES spectra recorded at a photon energy $h\nu = 65\,\text{eV}$. a) Constant energy map at $\varepsilon = -5.2\,\text{eV}$, integrated over $100\,\text{meV}$ (π-polarized light). Straight lines point out the true (orthorhombic) zone boundaries and dashed lines mark the tetragonal BZ. The thick blue line indicates the spectral cut at which the energy distribution map in b) (circular polarized light) was taken. c) Calculated spectral function. The dashed line indicates an arbitrary shift with respect to the measurement.

Up to an overall energy shift, excellent agreement is found between DFT calculations and data of the oxygen bands [Fig. 4.2 b) and c)]. A spectral cut through the bands at these high degeneracy points reveals a checkerboard-like structure in the constant energy (CE) map [Fig. 4.2 a)]. The orthorhombic zone centers Γ_i with $i = 1, 2, 3$ are identified.

Mott gap of Ca_2RuO_4

An estimate of the minimal insulating Mott gap is best discussed by integrating spectral weight over the whole projected BZ. As shown in Fig. 4.3 spectral weight is completely suppressed for $\varepsilon > -0.2\,\text{eV}$.
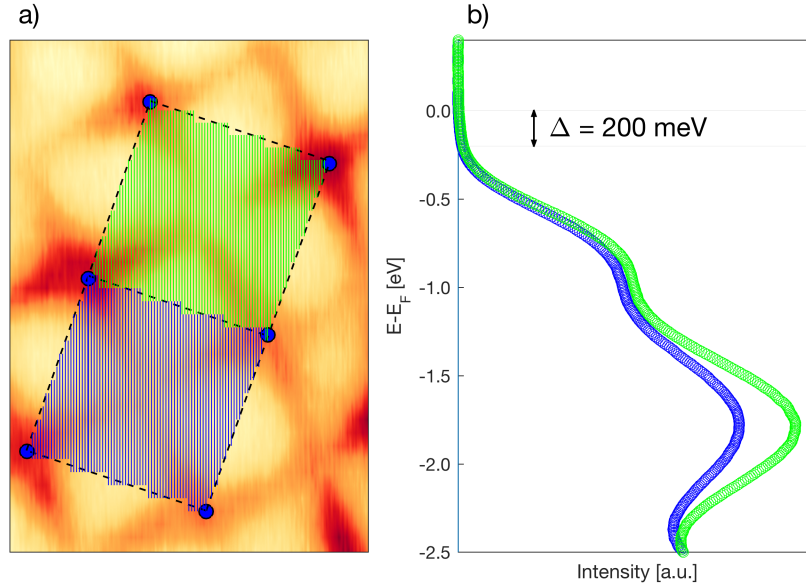
Fig. 4.3 a) CE map ($\varepsilon = -5.2\,\text{eV}$) and area of integration indicated in green and blue. b) Respective DOS. Complete suppression of spectral weight at approximately $\varepsilon = -0.2\,\text{eV}$.

This result underlines the Mott-insulating behavior of Ca214. The Mott gap, defining the energy scale between lower and upper Hubbard bands has previously been associated with the activation energy of $E_{\text{activ.}} = 0.4\,\text{eV}$[1] derived from resistivity measurements [58]. Assuming that the Fermi-level is centered approximately symmetrical between lower and upper Hubbard bands, the spectroscopic observation of $\Delta = E_{\text{activ.}}/2 \approx 0.2\,\text{eV}$ is in good agreement with the transport experiments [58].

4.2   Ruthenium bands

We now focus on the excitations closer to the Fermi-level. The structure of these bands is ruthenium-dominated and forms **the main topic of the thesis**. Fig. 4.4 a) shows an EDM with a broad and flat band found at $\varepsilon \sim -1.7\,\text{eV}$. Especially near the zone boundary, additional structure is observed closer to the Fermi-level at $\varepsilon \sim -0.8\,\text{eV}$. These two flat ruthenium bands (labeled β and α) are revealed as a clear double peak structure in the EDC at the

---

[1]Resistivity of activation-type insulating behavior: $\rho(T) \propto \exp(E_{\text{activ.}}/2k_BT)$

S-point [Fig. 4.4 c)]. The third structure, labeled γ, is the fast dispersing band at $\varepsilon \sim -2.2$ eV, indicated in the MDC at $\varepsilon_{\mathrm{MDC}} = -2.4$ eV in Fig. 4.4 a). Estimated from several MDC's, the band velocity yields $v_\gamma = 2.6 \pm 0.4$ eV Å.
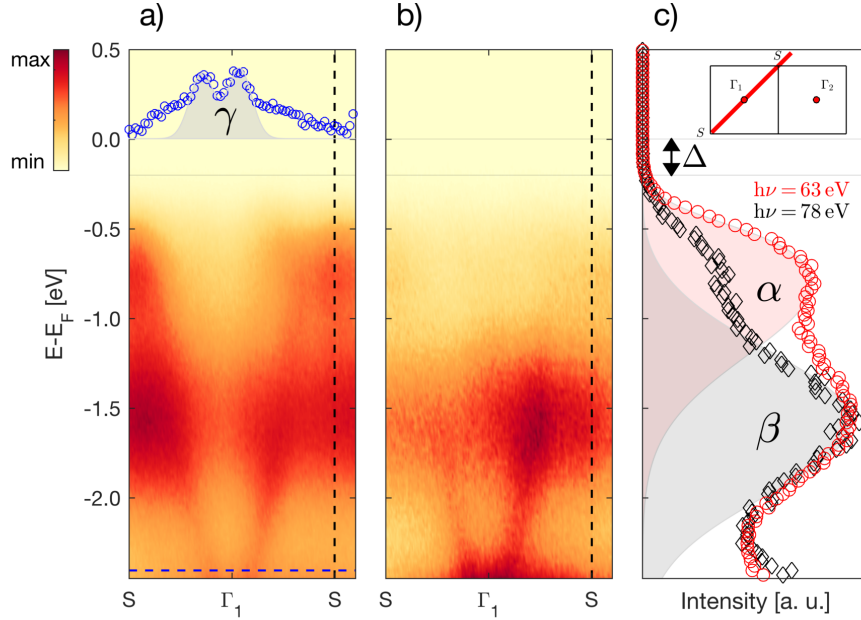

Fig. 4.4 Photoemission spectra recorded along the high-symmetry direction $\Gamma_1 - S$ [inset in c)] for incident photon energies (circular polarized) and spectral cuts as indicated. a) EDM at $h\nu = 63$ eV with an MDC ($\varepsilon = -2.4$ eV) in the inset. b) EDM at $h\nu = 78$ eV. c) EDC's at the *S*-point, displaying intensity variations of the α-band.

By changing the photon energy from 63 eV to 78 eV (circular polarized light), the α-band gets strongly suppressed, while the β- and γ-bands are still clearly visible. So far no assumptions on the orbital band character have been made. Although details can vary depending on methodology, band structure calculations of Ca214 commly find a single fast dispersing branch, centered around Γ [59], [60], [61]. Our DFT calculation [see Fig. 4.11, will be discussed in greater detail] reveal that the orbital composition of this fast dispersing band is predominantely of d_{xy} character.

Conclusion: The in-plane d_{xy}-orbitals create the γ-band.

4.3   Matrix element effects

In this part of the discussion, the focus is on the change of spectral weight distribution depending on light polarization and photon energy. These changes are subject to matrix element effects. Fig. 4.5 summarizes this behavior.
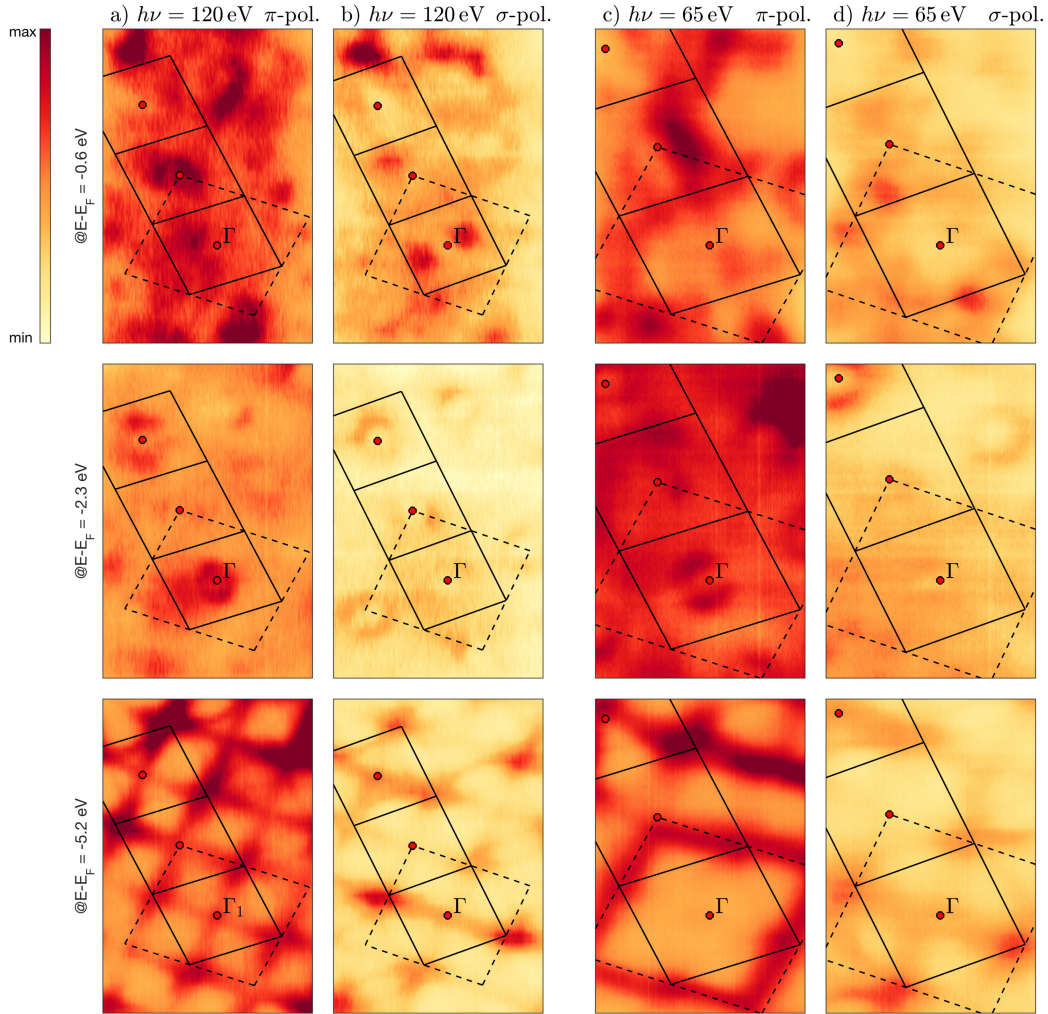
Fig. 4.5 Constant energy maps at different energies $E - E_F$ as indicated. Maps in the top row cut through the α-band, in the middle row through the γ-band and in the last row the maps probe oxygen bands. Columns correspond to different photon energies and light polarization. Zone boundaries are marked by the straight lines. The dashed zone correspond to the tetragonal symmetry.

It shows CE maps taken at different photon energies and polarization as indicated without alignment along any high symmetry direction. The CE maps in the first row are taken at $\varepsilon = -0.6\,\text{eV}$, cutting through the α-band. In the second row, $\varepsilon = -2.3\,\text{eV}$, we probe the γ-band and in the third row at $\varepsilon = -5.2\,\text{eV}$, we are deep in the oxygen bands where the spectral weight forms a checker board-like structure. Γ-points can still be identified in the CE maps of the γ-band but for the α-band, no regularity is observed. Photo emission matrix elements on the α-band are therefore very complex. In the following analysis, polarization and photon energy dependence are studied in a more systematic fashion. High symmetry boundaries of the BZ were well aligned with the direction of the incident light.
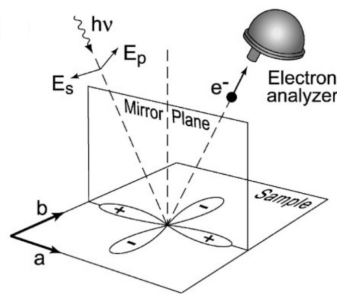
Polarization

The polarization dependence is analyzed for the ruthenium bands along the high-symmetry cut $\Gamma_2 - S$, for which this effect is most severe. Fig. 4.6 a) and b) are spectra taken at $\pi-$ and σ-polarization, respectively. EDC's [see Fig. 4.6 c)] reveal that the α-band is affected the most, relatively to the β-band.
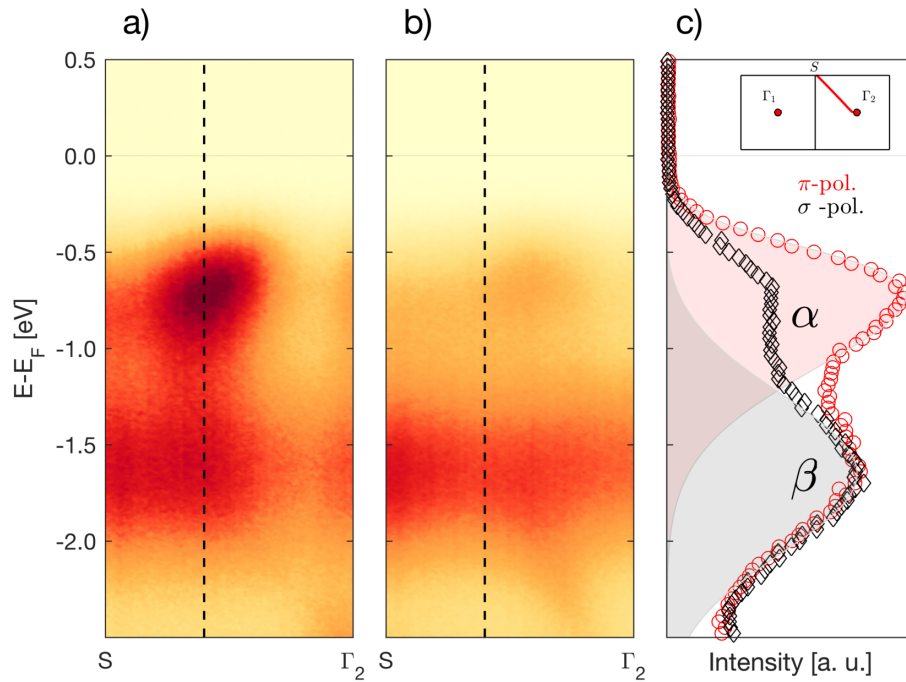

Fig. 4.6 Photoemission spectra recorded along the high-symmetry direction $\Gamma_2 - S$ [inset in c)] for lights polarizations ($h\nu = 63$ eV) and spectral cuts as indicated. a) EDM for p-polarization and in b) for s-polarization. c) EDC's as indicated, again displaying intensity variations of the α-band.

In the experiment, the detector slit was perpendicular to the plane, spanned by the incident light and the sample surface normal. This is the *horizontal* slit geometry, for which an overall mirror plane, spanned by the light and the photoelectron cannot be constructed.

Fig. 4.7 Illustration of the symmetries in the photoemission process with a $d_{x^2-y^2}$-orbital.

Hence, a discussion of the polarization dependence by photoemission selection rules in the spirit of Damascelli *et al.* [Fig. 4.7] [42] is not possible. An alternative approach to the polarization dependence is given by the $\mathbf{A} \cdot \mathbf{p}$-approach to the matrix element introduced in chapter 3.3. Fig. 4.8 summarizes the outcome.
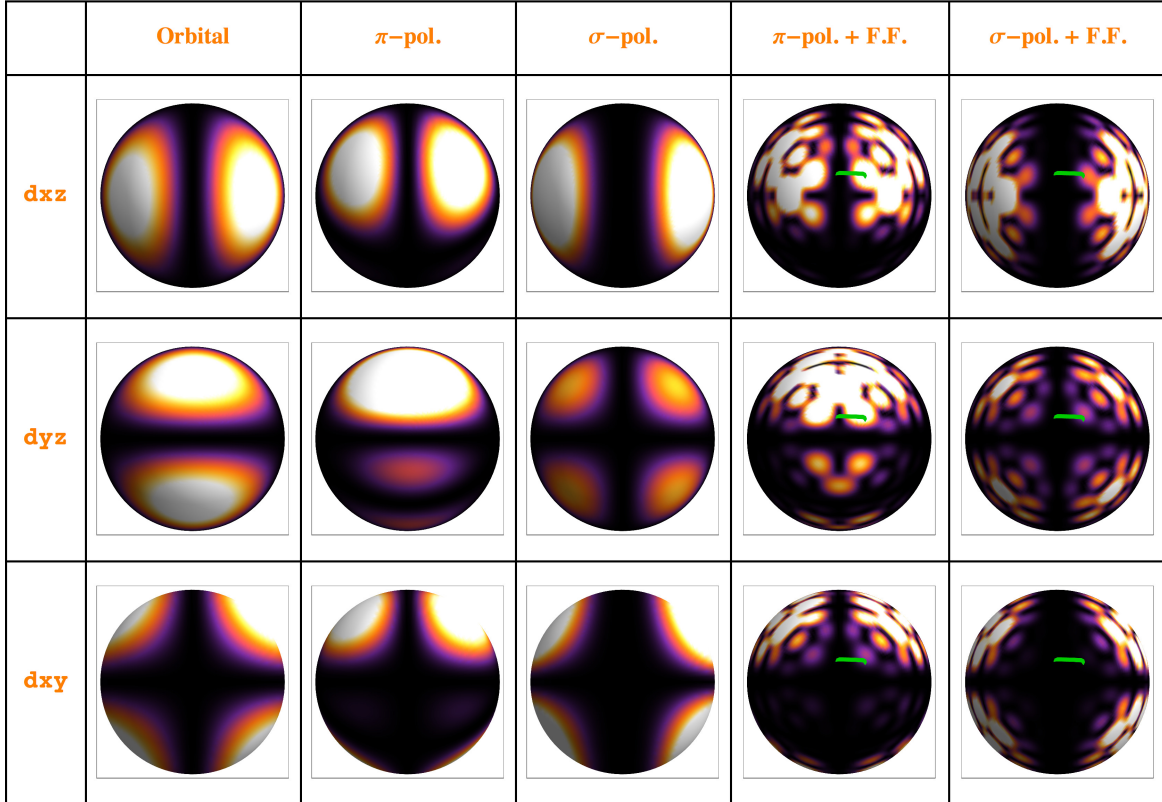

Fig. 4.8 Angular distribution of $|\mathcal{M}(\theta_k, \varphi_k)|$. Column one: atomic orbitals. Column two and three: Light source from bottom towards the center with incidence angle $\alpha = 45°$. Column four and five: Form factor of the unit cell is included with detector slit as indicated.

First column shows the angular distribution of *d*-orbitals, indicated to the left. Second and third columns are angular distributions $|\mathcal{M}(\theta_k, \varphi_k)|$ of photoelectrons with a light source directed from bottom to the center at incidence angle $\alpha = 45°$. Light polarization is given in the top row. In the last two rows, the form factor of the unit cell is taken into account. The spectral cut shown in the inset of Fig. 4.6 c) corresponds to the green curve in Fig. 4.8. This simple model suggests almost no intensity for d_{xy} for both polarization configurations. For the out-of-plane d_{xz}, d_{yz} orbitals, it can be inferred that their spectral weight distribution generally weakens when changing from π- to σ-polarization. This behavior is captured in Fig. 4.5. However, Bradshaw and Woodruff [62] recently pointed out that it is not proven that the plane wave final state approximation (as used in this model) is nearly equivalent to

the more correct spherical wave approximation in photoemission experiments. Thus, taking spherical waves as final states would be a natural improvement of the model.

Photon energy dependence

The photon energy dependence is studied along the $\Gamma_1 - S$ direction by using the $\mathbf{A} \cdot \mathbf{x}$-approach from chapter 3.3 to analyze the data. In the calculations a phase has been introduced which is discussed in greater detail in the appendix. Figure 4.9 shows a compilation of ARPES spectra along the high-symmetry cut $\Gamma_1 - S$. Intensity of the γ-band has been integrated for all spectra, from which we expect d_{xy}-behavior [see green boxes in Fig. 4.9]. This has been also done for the α-band [blue boxes], expecting a different behavior due to the polarization comparisons [Fig. 4.6].
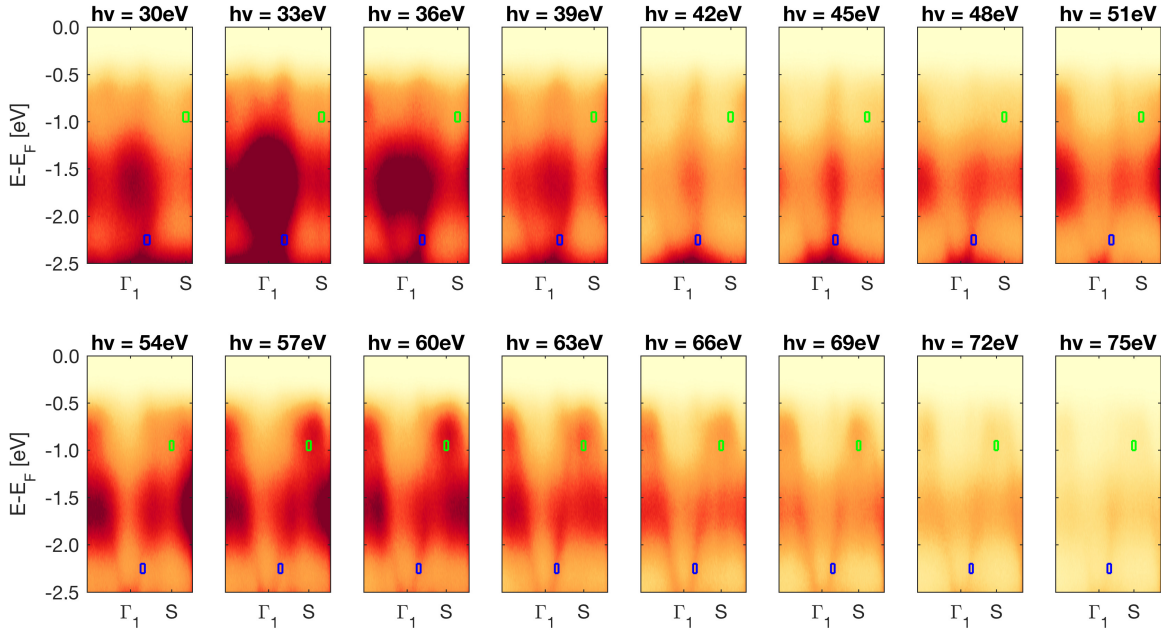
Fig. 4.9 Compilation of spectra along $\Gamma_1 - S$, recorded at different photon energies as indicated. Boxes in blue and green are boundaries within intensity is integrated.

Results are plotted in Fig. 4.10 a) and b), for which the colors green and blue correspond to those of Fig. 4.9. On the one hand, data points in a) display weak oscillations with a monotonic downward-trend for higher photon energies, indicated by the straight line. On the other hand, the plot in b) reveals strong oscillations with maxima at approximately $h\nu = 33$ eV and $h\nu = 60$ eV. Qualitatively, a good agreement of model and measurement is found [Fig. 4.10].
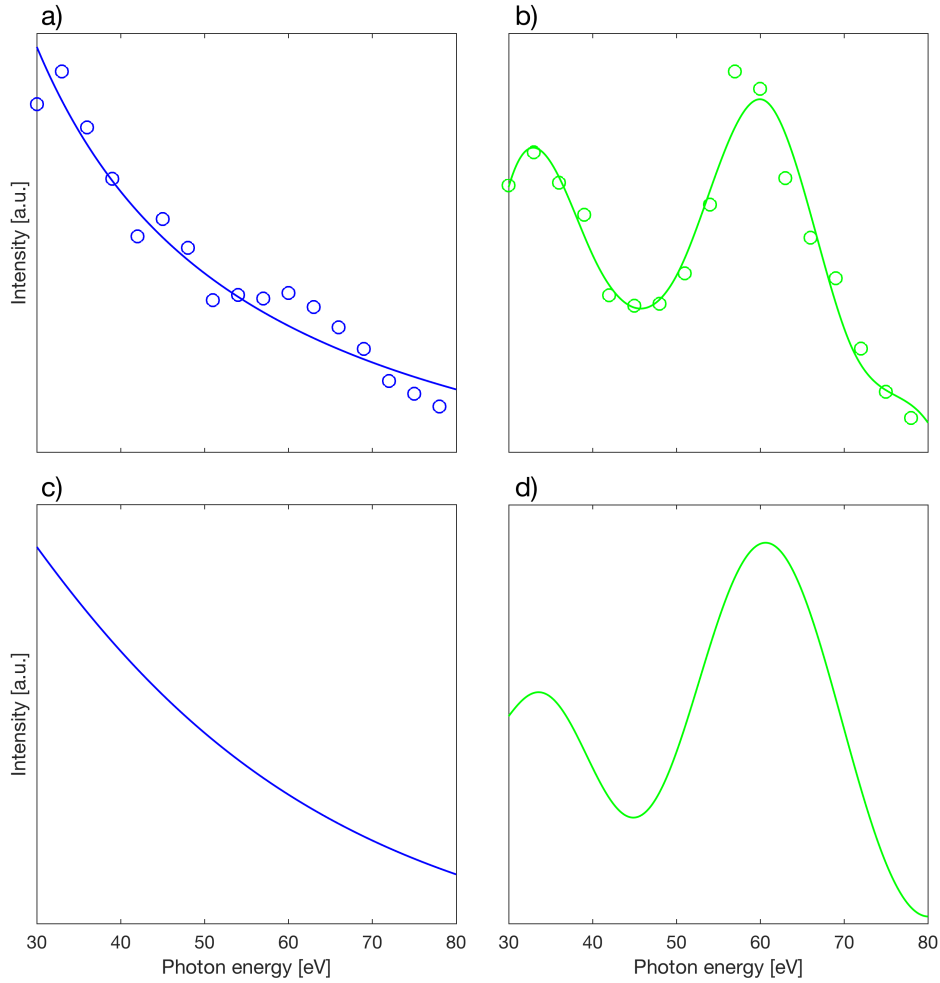
Fig. 4.10 a) & b): Result of the integration process, showed in Fig. 4.9. Rings are data points. A line to guide the eye is added. Colors green and blue correspond to the boxes in Fig. 4.9. c) Calculated matrix element for d_{xy}-orbitals. d) Calculation for d_{xz}, d_{yz}-orbitals.

Increasing the photon energy, implies that we are probing higher BZ's, stacked along k_z. Following references [59], [60], [61], spectral function effects are not expected and therefore no variations along k_z, originating from band dispersion. A weak out-of-plane dispersion can be intuitively understood by recalling that Ca214 has a layered crystal structure with a long c-axis and thus little overlap of the out-of-plane orbitals. Also the calibration curve of the photo diode used in experiment has a slightly upward, monotonic behavior for this photon energy range and thus cannot be attributed to the decreasing trend of the blue data.

Photon energy dependence of the bands reveal distinct behavior which can be compared to the results of the model.

Conclusion: The α-band has d_{xz}, d_{yz} character and the γ-band has d_{xy} character.

4.4   Multi-gap scenario

In this final part, the first-principle band structure calculations will be compared to larger data set of the ruthenium bands. Fig. 4.11 a) presents a compilation of ARPES spectra, recorded along high-symmetry directions as indicated in the CE-map in b). Light is circular polarized with a photon energy of 65 eV, close to the maximum in Fig. 4.10 b).
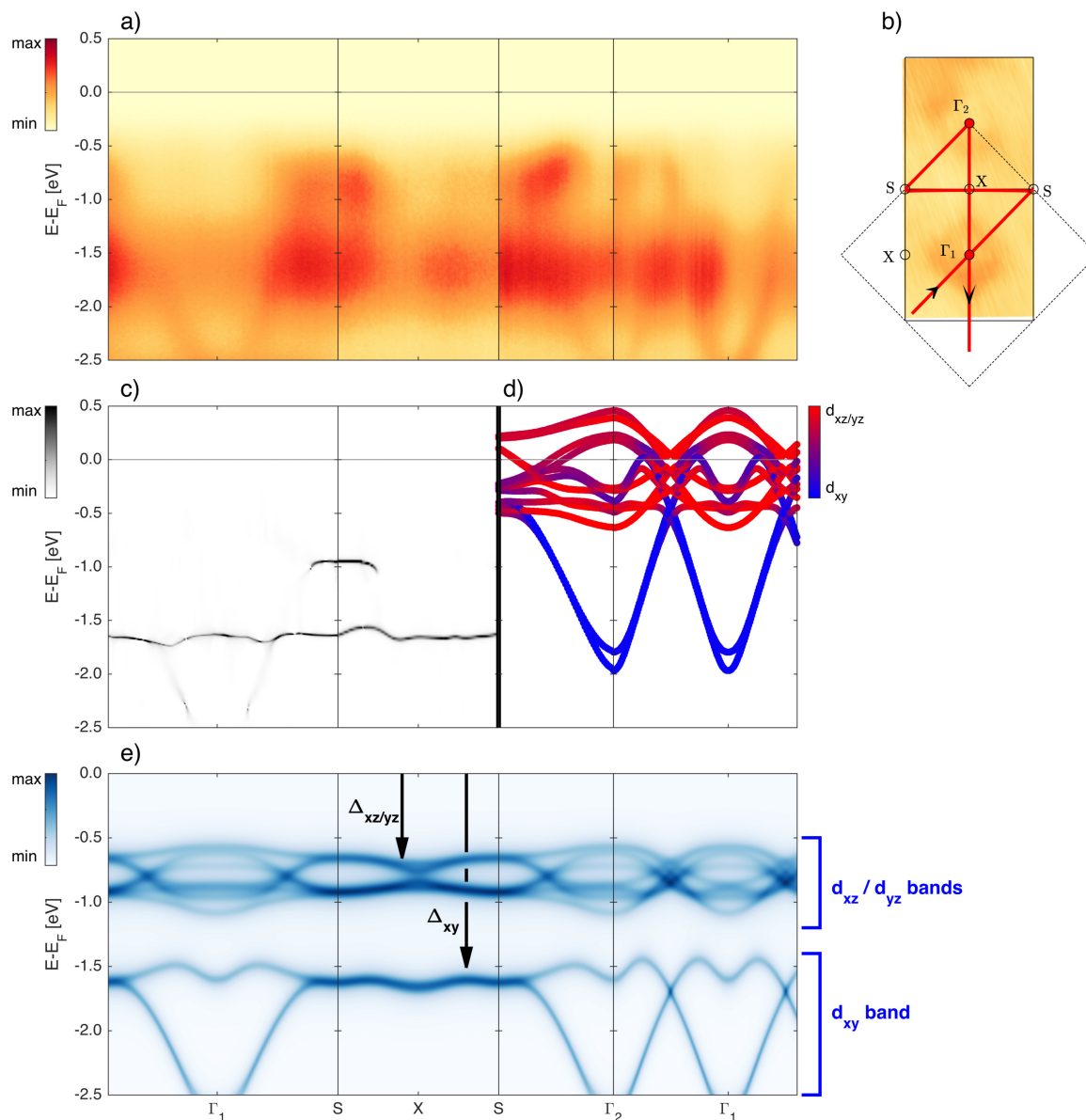
Fig. 4.11 a) Compilation of ARPES spectra along high-symmetry directions, denoted at the bottom of the figure. b) CE-map and path of the spectral cuts (straight line: orthorhombic zone, dashed line: tetragonal zone). c) Curvature map of two spectra. d) Band structure calculations of the orbital characters. e) Calculated spectral function including orbital dependent Mott gaps.

The flat β-band extends over the whole BZ. Closer to the Fermi-level, the α-band reveals its structure. As expected, the γ-band evolves around Γ_1. The orthorhombic crystal structure imposes a band folding, seen as γ-band replica around Γ_2 in the next orthorhombic zone [Fig. 4.11 a & b)]. Representative curvature maps along $\Gamma_1 - S - X$ [Fig. 4.11 c)] reveal no clear evidence, that the γ-band is found in between the α and β bands. Also demonstrated in Fig. 4.6, it is absent for $h\nu = 78\,\mathrm{eV}$.

Having explored the orbital character of the bands, the band structure is discussed in a more general context. Fig. 4.11 d) displays DFT+LDA calculations including spin-orbit coupling but without Coulomb interaction. The structure of quasiparticle band dispersions are reproduced but lie on energy scales at the Fermi-level indicating absence of Mott physics. Introducing a uniform U, acting equally on all orbitals, results in a single spectral Mott gap which cannot explain the two different energy scales associated to the α- and β-bands. Thus, the observed band structure suggests that at least two energy scales are involved in the Mott insulating phase. To mimic this effect on a phenomenological level, orbital selective Mott gaps are included in the first principle calculations [detail in the appendix]. It is not obvious whether Mott physics would acts strongest on the d_{xy} or on the d_{xz}, d_{yz} orbitals. The data analysis presented so far, suggests how a disentanglement of the orbital characters may be realized. Furthermore, quantum oscillation experiments on Sr_2RuO_4 suggest that the γ-band with d_{xy} orbital character is more strongly dressed [19], [63]. For these reasons, a stronger Mott gap acting on d_{xy}-orbitals ($\Delta_{xy} = 2.15\,\mathrm{eV}$) is included than on the the d_{xz}, d_{yz} orbitals ($\Delta_{xz/yz} = 0.50\,\mathrm{eV}$) as shown in Fig. 4.11 e). This minimalistic approach reproduces qualitatively the observed band structure.

4.5   Conclusions & Outlook

In conclusion, I have shown how orbital characters may be associated to the bands observed with angle resolved photoemission spectroscopy. The fast dispersing γ-band has predominantely d_{xy} while the α-band has more $d_{xz,yz}$-character. Spectral weight separation of the α and β bands suggest a scenario where two Mott gaps are included in the first principle calculations presented.

Conclusion: The paramagnetic Mott insulating state of Ca_2RuO_4 concludes the involvement of two insulating energy scales.

On a theoretical level, this can be realized in different scenarios, that typically involve orbital separation. It has, for example, been suggested that the particular crystal field environment of Ca214 favors a fully filled d_{xy}-band and half filled d_{xz}, d_{yz}-band [64]. The narrow half-filled bands get localized. As a result, the system will be a combined band and Mott insulator. This

scenario would naturally produce orbital dependent insulating scales. The orbital selective Mott scenario also results in two insulating energy scales. Here, a sufficiently strong Hund's coupling triggers orbital specific transitions on the different orbitals [see chapter 2.4]. J equalizes orbital occupation and induces Mott physics depending on their band-fillings. However, orbital depolarization can also be supported by spin-orbit coupling ($\Delta_{s.o.} \sim 200\,\mathrm{meV}$ [57]), mixing different orbitals. An indirect way to determine a distinction of these two scenarios, orbital selective Mott physics or mixed band and Mott insulator, is spin resolved ARPES[2]. When band occupation is saturated, the Pauli exclusion principle implies vanishing spin degrees of freedom. This should be captured in the spin polarization of the electronic bands, reflecting their filling number.
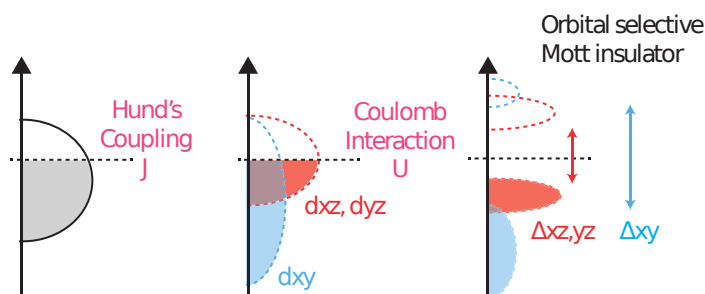
Fig. 4.12 Schematic DOS of an orbital selective Mott insulator transition. A delicate interplay of U and J might induce orbital dependent Mott physics.

It is to emphasize that the used DFT model is a minimalistic way to reproduce the observed band structure. For future theoretical analysis, more sophisticated models should be applied.

An orbital selective Mott phase suggests also the metal-insulator transition to be orbital dependent. ARPES experiments for different off-stoichiometric compositions of $Ca_{2-x}Sr_xRuO_4$ ($x = 0.1, 0.2, 0.3$) are important to shed light on this problem[3].

[2]Proposal accepted for beam time (September 2016) at the SIS beam line at SLS, PSI in Villigen, CH
[3]Proposal accepted for beam time (February 2017) at the I05 beam line at DLS in Oxford, UK

Appendix A

Modeling details

Photon energy dependence

For a given incident photon energy, the ARPES experiment probes a projected part of the BZ of the given sample. Tuning the photon energy in ARPES translates into a variation of k_z [Fig. A.1]. This influences the electron final state and therefore matrix element effects. Fig. A.2 represents calculations following the $\mathbf{A} \cdot \mathbf{p}$-approach [chapter 3.3]. Two maxima can be inferred for the d_{xz}, d_{yz} orbitals which approximately match the periodicity observed for the α-band. The form factor allows the interpretation of the oscillations as an interference effect but the calculation does not reproduce the data.
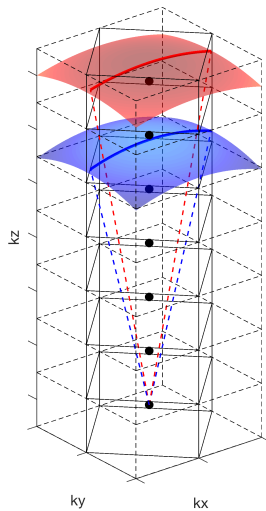
Fig. A.1 Schematic representation of higher BZ's with projections for a given photon energy as indicated. $h\nu_{\mathrm{blue}} < h\nu_{\mathrm{red}}$.
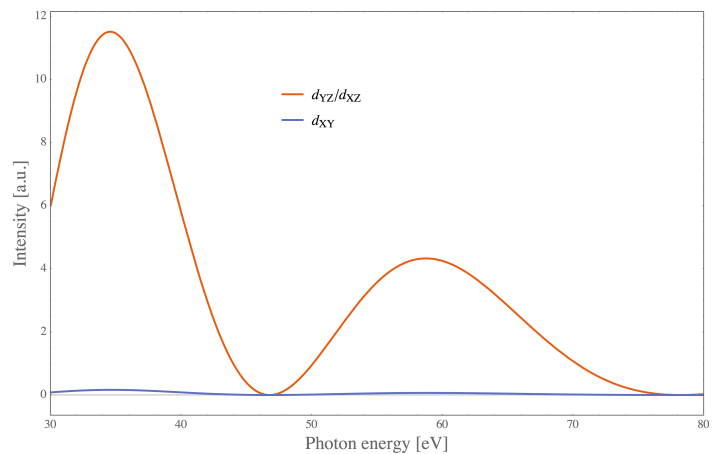
Fig. A.2 Schematic representation of higher BZ's with projections for a given photon energy as indicated. $h\nu_{\mathrm{blue}} < h\nu_{\mathrm{red}}$.

Starting from the $\mathbf{A} \cdot \mathbf{x}$-approach, a phenomenological phase $e^{i(k_z c/2 + \phi_0)}$ to the z-component $\mathcal{M}_z$ is added according to Ref. [46]. Although the interpretation of the phase is not entirely clear, this approach has been successful to match ARPES data of Fe-based superconductors. The full matrix element is:

$$\mathcal{M}^{\delta} = \mathcal{M}_x^{\delta} + \mathcal{M}_y^{\delta} + \mathcal{M}_z^{\delta} \cdot e^{i(k_z c/2 + \phi_0)} \tag{A.1}$$

As outlined in the thesis, a good agreement of the data and simulation is found.

The oscillatory behavior can be also understood qualitatively. The radial part of the matrix element $\rho_\ell(k_f r)$ in equation (4.30) is the determined by the overlap of the atomic radial wavefunction (effective atomic number $Z_{\text{eff}} = 20$ was chosen) and the spherical besselfunction, coming from the partial wave expansion of the approximated plane wave final state. In a wide photon energy range, we may neglect higher orders of $\ell > 1$ ($\rho_1(k_f r) \gg \rho_3(k_f r)$). For a fixed magnetic quantum number $m = \lambda$ the matrix element $\mathcal{M}$ associated to λ reads:

$$\mathcal{M}^{\lambda}(\theta_k, \varphi_k) = \sum_{\alpha = x,y,z} \mathcal{M}_{\alpha}^{\lambda}(\theta_k, \varphi_k) = \sum_{\alpha = x,y,z} D_{\alpha} \Upsilon_{\alpha}^{\lambda}(\theta_k, \varphi_k)$$
$$\Upsilon_{\alpha}^{\lambda}(\theta_k, \varphi_k) \simeq \rho_1(k_f r) \sum_{m=-1}^{1} Y_1^m(\theta_k, \varphi_k) f_{\alpha}^{\lambda}(1, m). \tag{A.2}$$

The phase in the total matrix element results in an oscillatory behavior for non-vanishing z-component $\mathcal{M}_z^{\lambda}$. It is enough to consider for what λ the sum of Gaunt coefficients $\sum_{m=-1}^{1} f_{\alpha}^{\lambda}(1, m)$ in equation A.2 vanishes. Dropping all angular dependencies (θ, φ) in the notation with $\alpha = \{x, y, z\}$:

$$f_{\alpha}^{\lambda}(1, m) = \oint_{S^2} d\Omega \, Y_{\ell=1}^{m*} p_{\alpha} Y_{\ell'=2}^{\lambda},$$
$$p_x = x/r = \sqrt{\frac{1}{2}} (Y_1^{-1} - Y_1^1)$$
$$p_y = y/r = i\sqrt{\frac{1}{2}} (Y_1^{-1} + Y_1^1) \tag{A.3}$$
$$p_z = z/r = Y_0^1$$

For $\mathcal{M}^{d_{xy}} = i\sqrt{\frac{1}{2}} (\mathcal{M}^{-2} - \mathcal{M}^2)$ the z-Gaunt coefficients are:

$$f_z^{\pm 2}(1,-1) = \oint_{S^2} \mathrm{d}\theta\,\mathrm{d}\varphi\,\sin\theta\,Y_1^{-1*}Y_1^0 Y_2^{\pm 2} \sim \oint_{S^2} \mathrm{d}\theta\,\mathrm{d}\varphi\,\sin^4\theta\cos\theta\,\overbrace{e^{i\varphi(1\pm 2)}}^{\oint \mathrm{d}\varphi = 0} = 0$$

$$f_z^{\pm 2}(1,0) = \oint_{S^2} \mathrm{d}\theta\,\mathrm{d}\varphi\,\sin\theta\,Y_1^{0*}Y_1^0 Y_2^{\pm 2} \sim \oint_{S^2} \mathrm{d}\theta\,\mathrm{d}\varphi\,\sin^3\theta\cos^2\theta\,\overbrace{e^{\pm 2i\varphi}}^{\oint \mathrm{d}\varphi = 0} = 0$$

$$f_z^{\pm 2}(1,+1) = \oint_{S^2} \mathrm{d}\theta\,\mathrm{d}\varphi\,\sin\theta\,Y_1^{1*}Y_1^0 Y_2^{\pm 2} \sim \oint_{S^2} \mathrm{d}\theta\,\mathrm{d}\varphi\,\sin^4\theta\cos\theta\,\overbrace{e^{i\varphi(1\mp 2)}}^{\oint \mathrm{d}\varphi = 0} = 0$$

Thus to first order, $\mathscr{M}_z^{d_{xy}} = 0$ and therefore no oscillatory character is assigned to d_{xy}-orbitals. Analogue for the other orbitals, $\mathscr{M}^{d_{yz}} = i\sqrt{\frac{1}{2}}\left(\mathscr{M}^{-1} + \mathscr{M}^1\right)$ and $\mathscr{M}^{d_{xz}} = \sqrt{\frac{1}{2}}\left(\mathscr{M}^{-1} - \mathscr{M}^1\right)$ the z-Gaunt coefficients are:

$$f_z^{\pm 1}(1,-1) = \oint_{S^2} \mathrm{d}\theta\,\mathrm{d}\varphi\,\sin\theta\,Y_1^{-1*}Y_1^0 Y_2^{\pm 1} \sim \oint_{S^2} \mathrm{d}\theta\,\mathrm{d}\varphi\,\overbrace{\sin^3\theta\cos^2\theta}^{\text{even}}\overbrace{e^{i\varphi(1\pm 1)}}^{+:\ \oint \mathrm{d}\varphi = 0} = f_z^{-1}(1,-1)$$

$$f_z^{\pm 1}(1,0) = \oint_{S^2} \mathrm{d}\theta\,\mathrm{d}\varphi\,\sin\theta\,Y_1^{0*}Y_1^0 Y_2^{\pm 1} \sim \oint_{S^2} \mathrm{d}\theta\,\mathrm{d}\varphi\,\sin^2\theta\cos^2\theta\,\overbrace{e^{\pm i\varphi}}^{\oint \mathrm{d}\varphi = 0} = 0$$

$$f_z^{\pm 1}(1,+1) = \oint_{S^2} \mathrm{d}\theta\,\mathrm{d}\varphi\,\sin\theta\,Y_1^{1*}Y_1^0 Y_2^{\pm 1} \sim \oint_{S^2} \mathrm{d}\theta\,\mathrm{d}\varphi\,\overbrace{\sin^3\theta\cos^2\theta}^{\text{even}}\overbrace{e^{i\varphi(1\mp 1)}}^{+:\ \oint \mathrm{d}\varphi = 0} = f_z^{+1}(1,+1)$$

Concluding finite $\mathscr{M}_z$ for d_{xz} and d_{yz} orbitals and therefore oscillatory behavior to first order. To summarize this result:

$$\langle \mathbf{k}_f | \mathbf{D}\cdot\mathbf{x} | d_{xy}\rangle_{h\nu} \approx const.$$
$$\langle \mathbf{k}_f | \mathbf{D}\cdot\mathbf{x} | d_{yz}\rangle_{h\nu} \neq const. \tag{A.4}$$
$$\langle \mathbf{k}_f | \mathbf{D}\cdot\mathbf{x} | d_{xz}\rangle_{h\nu} \neq const.$$

First principle calculations

All DFT calculations were performed by Prof. Titus Neupert[1], Dr. Tay-Rong Chang[2] and Prof. H.-T. Jeng[3].

We computed electronic structures using the projector augmented wave method [65], [66] as implemented in the VASP [67], [68], [69] package within the generalized gradient approximation (GGA) [70] schemes. Experimental lattice constants were used (a = 5.39, b = 5.59 and c = 11.77 Å). A $12 \times 10 \times 4$ Monkhorst-Pack k-point mesh was used in the computations with a cutoff energy of 400 eV. The spin-orbit coupling (SOC) effects are included self-consistently. In order to model Mott physics, we constructed first-principles tight-binding model Hamilton, where the tight-binding model matrix elements were calculated by projecting onto the Wannier orbitals [71], [72], [73] which used the VASP2WANNIER90 interface [74]. We used Ru t_{2g} orbitals to construct Wannier functions without using the maximizing localization procedure.

The resulting 24-band spin-orbit coupled model with Bloch Hamiltionian matrix $\hat{\mathscr{H}}_{\mathbf{k}}$ reproduces well the first principle electronic structure near the Fermi energy. To the Green's function of this thight-binding model we added the leading divergent $1/\omega$ term of the self-energy $\hat{\Sigma}(\omega) = (\hat{P}_{xy}\Delta_{xy} + \hat{P}_{xz,yz}\Delta_{xz,yz})/\omega + \mathscr{O}(\omega^0)$ in the Mott insulating regime, where $\hat{P}_{xy}$ and $\hat{P}_{xz,yz}$ are projectors on the d_{xy} and $d_{xz,yz}$ orbitals, respectively, while Δ_{xy} and $\Delta_{xz,yz}$ are the corresponding weights of the poles. From the Green's function $\hat{G}(\mathbf{k},\omega) = [\omega - \hat{\mathscr{H}} - \hat{\Sigma}(\omega)]^{-1}$ with the two adjustable parameters Δ_{xy} and $\Delta_{xz,yz}$ we obtained the spectral function $\mathscr{A}(\mathbf{k},\omega)$ by taking the trace over all orbital and spin degrees of freedom.

[1]Department of Physics, University of Zurich, Switzerland
[2]Department of Physics, National Tsing Hua University, Hsinchu 30013, Taiwan
[3]Institute of Physics, Academia Sinica, Taipei 11529, Taiwan

References

[1] J.G. Bednorz and K.A. Müller. Possible high tc superconductivity in the Ba-La-Cu-O system. *Zeitschrift für Physik B*, 64:189–193, 1986.

[2] Y. Maeno *et al.* Superconductivity in a layered perovskite without copper. *Nature*, 372:532–534, 1994.

[3] Myron B. Salamon and Marcelo Jaime. The physics of manganites: Structure and transport. *Rev. Mod. Phys.*, 73:583–628, 2001.

[4] Y. Wang *et al.* Spin entropy as the likely source of enhanced thermopower in $Na_xCo_2O_4$. *Nature*, 423:425–428, 2003.

[5] A. Georges *et al.* Strong correlations from Hund's coupling. *Annual Review of Condensed Matter Physics*, 4:137–178, 2013.

[6] V. I. Anisimov *et al.* Orbital-selective Mott-insulator transition in $Ca_{2-x}Sr_xRuO_4$. *Eur. Phys. J. B*, 25:191, 2002.

[7] E. Dagotto. Complexity in strongly correlated electronic systems. *Science*, 309(5732):257–262, 2005.

[8] L. D. Landau. The theory of a Fermi liquid. *Soviet Physics JETP*, 3(6), 1957.

[9] N.F. Mott. Discussion of the paper by de boer and verwey. *Proc. Phys. Soc.*, 49:72, 1937.

[10] N.F. Mott. The basis of the electron theory of metals, with special reference to the transition metals. *Proc. Phys. Soc. London*, 62:416, 1949.

[11] P. A. Lee *et al.* Doping a Mott insulator: Physics of high-temperature superconductivity. *Rev. Mod. Phys.*, 78:17–85, 2006.

[12] M. Imada et al. Metal-insulator transitions. *Rev. Mod. Phys.*, 70:1039–1263, 1998.

[13] S. Watanabe and M. Imada. Precise determination of phase diagram for two-dimensional hubbard model with filling- and bandwidth-control Mott transitions. *arXiv:cond-mat/0312671v1*, 2003.

[14] L. de' Medic *et al.* Janus-faced influence of hund's rule coupling in strongly correlated materials. *Phys. Rev. Lett.*, 107:256401, 2011.

[15] Y. Tokura and N. Nagaosa. Orbital physics in transition-metal oxides. *Science*, 288:462–468, 2000.

[16] E. Pavarini *et al.* Mott transition and suppression of orbital fluctuations in orthorhombic $3d^1$ perovskites. *Phys. Rev. Lett.*, 92:176403, 2004.

[17] L. de' Medici. Orbital-selective Mott transition out of band degeneracy lifting. *Phys. Rev. Lett.*, 102:126401, 2009.

[18] L. de' Medici. Hund's coupling and its key role in tuning multiorbital correlations. *Phys. Rev. B*, 83:205112, 2011.

[19] A. Mackenzie and Y. Maeno. The superconductivity of Sr_2RuO_4 and the physics of spin-triplet pairing. *Rev. Mod. Phys.*, 75:657–712, 2003.

[20] A.P. Mackenzie et al. Quantum oscillations in the layered perovskite superconductor Sr_2RuO_4. *Phys. Rev. Lett.*, 76:3786–3789, 1996.

[21] T. Oguchi. Electronic band structure of the superconductor Sr_2RuO_4. *Phys. Rev. B*, 51:1385–1388, 1995.

[22] S. Nakatsuji and Y. Maeno. Quasi-two-dimensional Mott transition system $Ca_{2-x}Sr_xRuO_4$. *Phys. Rev. Lett.*, 84:2666–2669, 2000.

[23] T.M. Rice and M. Sigrist. Sr_2RuO_4 : an electronic analogue of 3 he? *Journal of Physics: Condensed Matter*, 7(47):L643, 1995.

[24] J. Lee *et al.* Orbital-selective mass enhancements in multiband $Ca_{2-x}Sr_xRuO_4$ systems analyzed by the extended drude model. *Phys. Rev. Lett.*, 96:057401, 2006.

[25] A. Shimoyamada. Strong mass renormalization at a local momentum space in multiorbital $Ca_{1.8}Sr_{0.2}RuO_4$. *Phys. Rev. Lett.*, 102:086401, 2009.

[26] M. Neupane *et al.* Observation of a novel orbital selective Mott transition in $Ca_{1.8}Sr_{0.2}RuO_4$. *Phys. Rev. Lett.*, 103:097001, 2009.

[27] E. Gorelov *et al.* Nature of the Mott transition in Ca_2RuO_4. *Phys. Rev. Lett.*, 104:226401, 2010.

[28] T. Mizokawa *et al.* Spin-orbit coupling in the Mott insulator Ca_2RuO_4. *Phys. Rev. Lett.*, 87:077202, 2001.

[29] T. Hotta and E. Dagotto. Prediction of orbital ordering in single-layered ruthenates. *Phys. Rev. Lett.*, 88:017201, 2001.

[30] Z. Fang *et al.* Orbital-dependent phase control in $Ca_{2-x}Sr_xRuO_4$. *Phys. Rev. B*, 69:045116, 2004.

[31] H. Hertz. Über einen Einfluss des ultravioletten Lichtes auf die electrische Entladung. *Annalen der Physik*, 33:983, 1887.

[32] P. Lenard. Über die lichtelektrische Wirkung. *Annalen der Physik*, 8:147, 1902.

[33] A. Einstein. Über einen die Erzeugung und Verwandlung des Lichtes betreffenden heuristischen Gesichtspunkt. *Annalen der Physik*, 17:132, 1905.

[34] R. G. Steinhardt. X-ray photoelectron spectrometer for chemical analysis. *Anal. Chem.*, 23(11):1585, 1951.

[35] K. Siegbahn *et al. ESCA: Atomic, Molecular and Solid State Structure by Means of Electron Spectroscopy*. Almquist and Wiksells, Uppsala, 1967.

[36] H. Y. Fan. Theory of photoelectric emission from metals. *Phys. Rev.*, 68:43, 1945.

[37] C. N. Berglund and W. E. Spicer. Photoemission studies of copper and silver: Theory. *Phys. Rev.*, 136(A):1030, 1964.

[38] P. J. Feibelman and D. E. Eastman. Photoemission spectroscopy—correspondence between quantum theory and experimental phenomenology. *Phys. Rev. B*, 10:4932, 1974.

[39] Randeria *et al.* Momentum distribution sum rule for angle-resolved photoemission. *Phys. Rev. Lett.*, 74:4951, 1995.

[40] M. P. Seah and W. A. Dench. Quantitative electron spectroscopy of surfaces: A standard data base for electron inelastic mean free paths in solids. *Surface and Interface Analysis*, 1:2–11, 1979.

[41] S. Hüfner. *Photoelectron Spectroscopy: Principles and Applications*. Springer, Berlin Heidelberg New York, 2003.

[42] A. Damascelli *et al.* Angle-resolved photoemission studies of the cuprate superconductors. *Rev. Mod. Phys.*, 75:473–, 2003.

[43] F. Baumberger, T. Greber, and J. Osterwalder. Fermi surfaces of the two-dimensional surface states on vicinal cu(111). *Phys. Rev. B*, 64:195411, 2001.

[44] R. Monnier. *Notes from solid state theory lecture*. UZH.

[45] S. Moser. An experimentalist's guide to the matrix element in angle resolve photoemission. *to be published*.

[46] X.-P. Wang *et al.* Orbital characters determined from Fermi surface intensity patterns using angle-resolved photoemission spectroscopy. *Physical Review B*, (85):214518, 2012.

[47] S. Nakatsuji and Y. Maeno. Synthesis and single-crystal growth of $Ca_{2-x}Sr_xRuO_4$. *Journal of Solid State Chemistry*, 156:26–31, 2001.

[48] J. Osterwalder. *Notes from electron spectroscopy lecture*. UZH.

[49] S. LaShell *et al.* Nonquasiparticle structure in the photoemission spectra from the Be(0001) surface and determination of the electron self energy. *Phys. Rev. B*, 61:2371–2374, 2000.

[50] T. Valla *et al.* Charge-density-wave-induced modifications to the quasiparticle self-energy in 2H-TaSe2. *Phys. Rev. Lett.*, 85:4759–4762, 2000.

[51] Christian Matt. *Master Thesis: The pseudogap phase in high-temperature superconductors.* ETH Zurich, 2012.

[52] P. Zhang *et al.* A precise method for visualizing dispersive features in image plots. *Review of Scientific Instruments*, (82):043712, 2011.

[53] M. D. Watson *et al.* Emergence of the nematic electronic state in FeSe. *Phys. Rev. B*, 91:155106, 2015.

[54] N. C. Plumb *et al.* Momentum-resolved electronic structure of the high-T_c superconductor parent compound $BaBiO_3$. *Phys. Rev. Lett.*, 117:037002, 2016.

[55] J. C. Campuzano *et al.* Extraction of the electron self-energy from angle-resolved photoemission data. *Physical Review B*, 60(10):7585, 1999.

[56] A. Dixit *et al.* Comparative analysis of coiflet and daubechies wavelets using global threshold for image de-noising. *IJAET*, 6(5):2247, 2013.

[57] C. G. Fatuzzo and J. Chang *et al.* Spin-orbit-induced orbital excitations in Sr_2RuO_4 and Ca_2RuO_4: A resonant inelastic x-ray scattering study. *Phys. Rev. B*, 91:155104, 2015.

[58] S. Nakatsuji *et al.* Mechanism of hopping transport in disordered Mott insulators. *Phys. Rev. Lett.*, 93:146401, 2004.

[59] K. Park. Electronic structure calculations for layered $LaSrMnO_4$ and Ca_2RuO_4. *Journal of Physics: Condensed Matter*, 13(41):9231, 2001.

[60] G.-Q. Liu. Spin-orbit coupling induced Mott transition in Ca_2RuO_4 ($0 \leq x \leq 0.2$). *Phys. Rev. B*, 84:235136, 2011.

[61] S. Acharya *et al.* Structural distortion, effective dimensionality, spin fluctuations and quantum criticality. *arXiv: 1605.0525*, 2016.

[62] A. M. Bradshaw and D. P. Woodruff. Molecular orbital tomography for adsorbed molecules: is a correct desription of the final state really unimportant? *New Journal of Physics*, 17(013033), 2015.

[63] J. Mravlje *et al.* Coherence-incoherence crossover and the mass-renormalization puzzles in Sr_2RuO_4. *Phys. Rev. Lett.*, 106:096401, 2011.

[64] A. Liebsch and H. Ishida. Subband filling and Mott transition in $Ca_{2-x}Sr_xRuO_4$. *Phys. Rev. Lett.*, 98:216403, 2007.

[65] P. E. Blöchl. Projector augmented-wave method. *Phys. Rev. B*, 50:17953–17979, 1994.

[66] G. Kresse. and D. Joubert. From ultrasoft pseudopotentials to the projector augmented-wave method. *Phys. Rev. B*, 59:1758–1775, 1999.

[67] G. Kresse and J. Hafner. Ab initio molecular dynamics for open-shell transition metals. *Phys. Rev. B*, 48:13115–13118, 1993.

[68] G. Kresse and J. Furthmüller. Efficiency of ab-inito total energy calculations for metals and semiconductors using a plane-wave basis set. *Computational Materials Science*, 6:15–50, 1996.

[69] G. Kresse and J. Furthmüller. Efficient iterative schemes for ab initio total-energy calculations using a plane-wave basis set. *Phys. Rev. B*, 54:11169–11186, 1996.

[70] J. P. Perdew *et al.* Generalized gradient approximation made simple. *Phys. Rev. Lett.*, 77:3865–3868, 1996.

[71] N. Marzari and D. Vanderbilt. Maximally localized generalized Wannier functions for composite energy bands. *Phys. Rev. B*, 56:12847–12865, 1997.

[72] I. Souza *et al.* Maximally localized Wannier functions for entangled energy bands. *Phys. Rev. B*, 65:035109, 2001.

[73] A. A. Mostofi *et al.* A tool for obtaining maximally-localised Wannier functions. *Computational Physics Communications*, 178:685–699, 2008.

[74] C. Franchini *et al.* Maximally localized Wannier functions in $LaMnO_3$ within PBE + U , hybrid functionals and partially self-consistent GW: an efficient route to construct ab initio tight-binding parameters for e_g perovskites. *Journal of Physics: Condensed Matter*, 24(23):235602, 2012.